Journal of Materials Chemistry A

Carbon Nanomaterials-Polymer Composites in Perovskite Solar Cells: Preparation, Properties and Applications

Journal:	*Journal of Materials Chemistry A*
Manuscript ID	TA-REV-03-2022-002175.R1
Article Type:	Review Article
Date Submitted by the Author:	01-May-2022
Complete List of Authors:	Dou, Qianqian; University of Louisville Whatley, Tanner; University of Louisville Syed, Tajamul Hussain; Wichita State University Wei, Wei; Wichita State University, Mechanical Engineering Wang, Hui; University of Louisville, Mechanical Engineering; University of Louisville, Conn Center for Renewable Energy Research

Carbon Nanomaterials-Polymer Composites in Perovskite Solar Cells: Preparation, Properties and Applications

Qianqian Dou,[a] Tanner Whatley,[a] Tajamul Syed,[b] Wei Wei[b], *Hui Wang*[a,c]

[a]Department of Mechanical Engineering Department, University of Louisville, 332 Eastern Parkway, Louisville, KY 40292, USA

[b]Department of Mechanical Engineering, Wichita State University, 1845 Fairmount Street, Wichita, KS 67260, USA

[c]Conn Center for Renewable Energy Research, University of Louisville, 216 Eastern Parkway, Louisville, KY 40208, USA

* Corresponding authors emails: hui.wang.1@louisville.edu; wei.wei@wichita.edu

Keywords: Perovskite solar cell, Composite, Functionalization, Carbon, Graphene

Abstract

Perovskite solar cell (PSC) is a rising star in the photovoltaic industry which achieves an enormous breakthrough in terms of efficiency from an initial 3.8% in 2009 to 25.7% in 2021. The major challenge to bring perovskite solar cells to pilot is the poor long-term device stability. The defects in perovskite and energy loss originated from charge recombination, limiting the efficiency of perovskite solar cells. Carbon-polymer composites which feature superb electrical conductivity, outstanding carrier mobility, remarkable flexibility and superior heat and moisture stability have attracted considerable attention to tackle these issues. With their multifunctional properties, carbon-polymer composites can play various roles in almost every component in perovskite solar cell architecture. In this review article, recent progress concerning the utilizations of carbon-polymer composites in different component in PSCs (i.e., perovskite additives, electrode, encapsulation layer and charge transport layer) is comprehensively overviewed. Then, the future research directions and opportunities toward high-performance perovskite solar cells utilizing carbon-polymer composites are presented.

1. Introduction

Using renewable energy resources (such as solar, wind and geothermal energy) rather than fossil fuels is the key to form a sustainable society and address the global warming issues resulted from the rapid population growth and industrialization[1-3]. Among various renewable resources, solar energy is abundant and environmental-friendly, and has immense potential to meet the rising energy demands. Photovoltaic devices that can convert solar energy into electric power, are necessitated for wider applications of solar energy[4, 5]. Crystalline silicon solar cells have dominated the photovoltaic (PV) market for decades; however, they suffer from the drawbacks of expensive raw materials and complicated manufacturing process.

A rising star in PV industry is hybrid perovskite solar cells (PSCs) that utilize metal halides (e.g., $MAPbX_3$ [$CH_3NH_3PbI_3$]) as the active material. For such PSCs, their power conversion efficiency (PCE) has experienced skyrocketing rise in the past decade (from 3.8% at 2009 to 25.7% at 2021)[6-10]. Recently, the lab-scale efficiency of 25.7 % for tin oxide electron transport layer (ETL) based solar cells is approaching the record efficiency of silicon solar cells[11]. Moreover, a potential efficiency of 31% of lead halide perovskite has been predicted by theoretical simulations[12]. Therefore, high efficiency, cost-effective, easy fabrication and industrial scalability are advantages of PSCs[13-16]. Nevertheless, one of the biggest challenges for PSCs is the long-term stability to maintain high efficiency, especially when subjected to environmental stresses such as moisture, UV light radiation and heating[17]. There are two negative factors resulting in the performance decay: (1) the photocatalytic degradation of perovskite materials due to the charge transport materials and metal diffusion originating from metal electrode[18-20]; (2) the ion migration caused by weak Coulomb force in perovskite lattice[21, 22].

To prevent the performance decay of PSCs, the recombination of electrons and holes within perovskite layers and interfaces should be minimized[23], thus carbon nanomaterials with excellent electrical and mechanical properties are highly promising to tackle the bottlenecks of PSCs[24]. For instance, the device with carbon materials (graphene, reduced graphene oxide (rGO), carbon nanotube (CNT), *etc.*) as spacer layer, additives or hole transport layer (HTL) yielded efficiency greater than 20% [25-27]. Several great reviews have summarized the utilization of carbon materials in PSCs and discussed their properties and roles[3, 5, 14, 28-31].

Although it is promising to introduce carbon materials into PSCs architecture, it is difficult to directly process high concertation of them through a surfactant-free solution-based approach[32]. Moreover, two-dimensional carbon materials may cause undesired charge

recombination due to the poor contact between layer-to-layer in PSC structure[33]. To maximize the advantages, one facile approach is to integrate carbon nanomaterials into polymer matrix to form composites[34], which display the synergistic effect between polymer and nanofillers to achieve improved properties over a wide range of conditions. There have been many reports on nanocomposites that utilize carbon materials (e.g., graphene and its derivatives and carbon nanotubes) in PSCs devices, nevertheless, a review that focuses on important discoveries regarding the carbon -polymer composite in PSCs is still lacking.

In this review, on the base of fundamental concepts of PSC structure, we firstly introduced the preparation methods of carbon-polymer nanocomposites, their conductive and mechanical properties as well as how they are integrated into PSCs structure. Then, the state-of-the-art results of using carbon nanomaterials-polymer composites in each component in PSC devices (e.g., perovskite layer, electron/hole transport layer and electrode) are then discussed. Finally, we highlight the perspectives for the future development of carbon nanomaterials-polymer composite based PSCs.

2. Working Principle and PSC Structure

A typical multilayered PSC contains five essential components: (1) a perovskite light absorber layer, (2) an electron transport layer (ETL), (3) a hole transport layer (HTL), (4) a transparent electrode and (5) a back electrode. As shown in **Figure 1a**, the general working principle is when exposed to sunlight, photons are captured and electron-hole pairs are generated in perovskite layer; then electrons move to the ETL meanwhile holes flow towards the HTL, followed by the electrons and holes extracted to the transparent electrode and a back electrode, respectively. Later, the transparent electrode and back electrode are connected to form an external circuit. The whole process is thermodynamically favorable when the valence and conduction band energy levels of the layers are aligned[35].

2.1 PSC device architectures

The device architectures for PSCs have undergone tremendous advancement within the last decade[36]. The architecture of PSCs is mainly classified into direct (n-i-p) and inverted (p-i-n) with either planar or mesoscopic structure, where n, i, and p stand for donor-type, intrinsic, and acceptor type semiconductors, respectively (**Figure 1b-d**). In planar regular (n–i–p) architecture, the ETL is deposited on a transparent conducting glass (transparent electrode), which is followed by depositing the perovskite active layer, then the HTL is deposited on top of perovskite film and topped by a metal contact[23, 30]. For mesoporous structure, it refers to the

use of a thin and compact titanium oxide (c-TiO_2) as a hole blocking layer, meanwhile a mesoporous TiO_2 or Al_2O_3 (m-TiO_2 or m-Al_2O_3) layer as electron-extraction scaffold to fill with perovskite materials[37]. In the inverted (p–i–n) configuration, the HTL is a bottom contact below perovskite layer while ETL is on the top and contacts with back electrode (e.g., Al). In general, a high-temperature sintering (450 ^{0}C) is required for the normal n-i-p and mesoporous structure that commonly employs TiO_2 as an ETL[38], while the p-i-n structure is more compatible with flexible devices because of its low processing temperatures[39, 40].

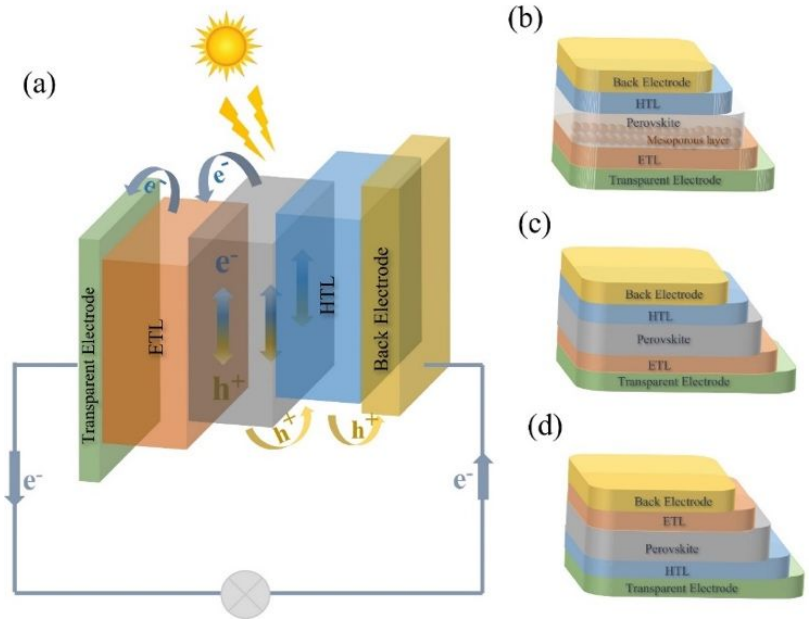

Figure 1 (a) General working principle of PSCs; device architectures of various PSCs: (b) mesoporous n-i-p (c) planar n-i-p and (d) inverted p-i-n structured PSCs.

2.2 Key Components in PSCs

The overall performance of PSC depends on several factors, the light harvesting separation efficiency of light absorber layer, charge separation at perovskite/HTL(ETL) interfaces and charge transport in perovskite, HTL and ETL, respectively.

2.2.1 Electrode

In PSCs, the transparent electrode and back electrode are used to collect the electrons and holes in PSCs, respectively. Transparent conductive oxides such as fluorine doped tin oxide (FTO) and tin doped indium oxide (ITO) are deposited on a glass substrate by a vacuum deposition technique to work as the transparent electrode. Moreover, conductive polymers, metal oxides, carbon nanotubes, graphene, metals also have been investigated as transparent electrode

materials[41-44]. For the back electrode in PSCs, metals (i.e., Au, Ag) and carbon-based materials are the most common materials used [45].

2.2.2 Perovskite-structured Materials

Metal halide perovskite takes on ABX_3, where A site is a monovalent cation that can be either organic cations MA ($CH_3NH_3^+$), or inorganic Cs^+, K^+, Rb^+ ions, or their mixture (organic-inorganic hybrid perovskite); B is divalent metal cation (Pb^{2+} or Sn^{2+}); and X represents halide anion (Cl^-, Br^- or I^-). The A-site cations are related to the band gap and crystal structure stability, while the B site (Pb *p* orbital) and X site (I *p* orbital) influence the band edge of perovskites [28, 46]. One main challenge that perovskite material facing is its long term stability, for instance, $CH_3NH_3PbI_3$ can degrade into PbI_2 and CH_3NH_3I in the presence of moisture, air and/or UV light[47].

2.2.3 Charge Transport Materials

Charge transport materials can be divided into electron transport material (ETM) and hole transport material (HTM). To ensure high efficiency of device, they are expected to hold the following features: high electron (hole) mobility, well-aligned energy levels with perovskite and electrode, high thermal stability, moisture resistant, as well as low cost and easy fabrication.

Electron Transport Layer (ETL). The popular inorganic ETL materials include metal oxides such as TiO_2, SnO_2 and ZnO[48]. For such materials, high temperature sintering is typically required to generate the electrically conducting phase (i.e., anatase for TiO_2). Besides, organic ETL materials such as fullerene (C_{60}) and its derivatives (i.e. [6,6]-phenyl-C61-butyric acid methyl ester (PCBM)) have been used in inverted PSCs [49].

Hole Transport Layer (HTL). The commonly organic HTL materials include spiro-OMeTAD [2,2',7,7'-tetrakis-(*N*,*N*-di-*p*-methoxyphenylamine)9,9'-spirobifluorene], P3HT [poly(3-hexylthiophene)], PTAA [poly(triarlyamine)], PANI [polyaniline], PTh [polythiophene], PEDOT [poly(3,4-ethylenedioxythiophene)], PEDOT:PSS [poly(3,4-ethylenedioxythiophene):poly(styrene sulfonate)], etc. Take PEDOT:PSS as example, it is a polyelectrolyte with the hydrophobic PEDOT and hydrophilic PSS, and is widely used for inverted PSCs due to its advantages of great transparency in visible range, high conductivity, and low process temperature[50]. However, the hygroscopic and acidic nature of PEDOT:PSS may cause the degradation and decomposition of the active layer and ITO electrode, and thus reduce the device stability[51-53].

Besides, inorganic HTL materials in PSCs include carbonaceous materials (e.g. graphene oxide (GO) and reduced graphene oxide (rGO)) due to their good electrical properties,

large specific surface area, and outstanding chemical and physical stability[54-56]. However, they also suffer from high oxygen content and poor solvent dispersion, which prevent their wide applications[54, 57].

3. Synthesis of Carbon-Polymer Nanocomposites

The carbon nanomaterials are featured with advantages of excellent electrical property and high stability[18, 58-61], however, the growth of nanostructured carbon sheets in large area with high quality and their incorporation into PSCs devices is difficult and expensive for practical applications. On the other side, polymers are relatively cheap and easy to process, but suffer from high resistance and poor mechanical properties[62-64]. Therefore, the preparation of carbon-polymer nanocomposite is a promising route to achieve synergistic properties, leading to the improvement on photovoltaic performance of assembled PSCs[65].

3.1 Carbon Materials

Graphene with 2D layer structure, first synthesized by Andre Geim and Konstantin Novoselov in 2004,[66] is considered as the building block for all carbon structure with other dimensionalities. It possesses good optical transparency (≈97.7%)[67], a high Young's modulus (≈1 TPa)[68], remarkable carrier mobility at room temperature (≈200 000 cm^2 V^{-1} s^{-1})[69], excellent thermal conductivity (≈5 × 103 W m^{-1} K^{-1})[70], and superior environmental stability[71]. Regarding its application in PSCs, one main challenge is to obtain uniform and thin graphene films[72]. Graphene oxide (GO), the most popular graphene derivative, is a single layer of graphene nanosheets functionalized with epoxy, carbonyl and hydroxyl groups[54, 73]. These functional groups enable GO to disperse easily in water, but also result in its poor electronic conductivity. Reduced graphene oxide (rGO) that hold less functional groups than GO have exhibited improvement in electronic characteristics[74, 75].

Carbon nanotubes (CNTs), 1D cylindrical carbon allotropes of graphene, discovered by Sumio Iijima[76], include single walled nanotubes (SWNTs) from the rolled single graphene sheet, and multi walled nanotubes (MWNTs) from the stacking of concentric layers of several graphene layers[77].

Carbon dots are considered as a kind of zero dimensional (0D) carbon dominated nanomaterials with sizes less than 10 nm[78]. Since the first report of carbon dots in 2004, their superior properties such as tunable photoluminescence, low toxicity and light stability have favored them wide applications[79]. The abundant functional groups of carbon dots make them prospects for modification application in perovskite solar cells and perovskite LEDs[80-82].

Carbon dots include graphene quantum dots (GQDs), carbon quantum dots (CQDs), carbon nanodots (CNDs) and carbonized polymer dots[78, 83], etc.

3.2 Preparation Methods of Carbon-Polymer Nanocomposites

So far, most polymer-carbon nanocomposites have been prepared through methods of (1) solution blending, (2) *in situ* polymerization, (3) melt mixing, and (4) coating. Other approaches include electrospinning, and electro-deposition, *etc*. For each method, the detail preparation process and examples are described as below, and their features are summarized and compared in Table 1.

3.2.1 Solution Blending

Solution blending is the most simple method for the nanocomposite preparation. In this method (**Figure 2a**), carbon nanomaterials and polymers are separately dispersed in a suitable solvent (water or organic) and then mixed; later, the solution mixture is coated on a substrate, followed by evaporation to remove the solvent. For the solvent blending method, one critical step is to obtain the homogeneous dispersion of carbon nanomaterials in the polymer, achieving the strong interaction and adhesion between each other. To prevent the self-aggregation of graphene or carbon nanotubes, it is important to carefully select appropriate solvents to dissolve the host polymer and carbon nanomaterials[65]. For examples, Han et al. chose chlorobenzene (C_6H_5Cl) to disperse PMMA [poly(methyl methacrylate)] and rGO, then sonicated the mixture[84]; Zheng et al. prepared a compact CNTs-P3HT film *via* dispersing them in C_6H_5Cl and followed by the sonification and stirring[85]. For some water-soluble polymers such as PEDOT:PSS, deionized (DI) water is used as the solvent to dissolve the polymer and graphene oxide (GO); either directly adding GO powder into PEDOT:PSS aqueous solution[86] or mixing GO in water dispersion with PEDOT:PSS solution[51].

In addition to the solvent selection, other facial approaches to facilitate the formation of homogeneous mixture solution include: (1) the modification of the carbon nanostructures and (2) the functionalization of polymers. In the *first* way, it involves grafting polymer chains on the surface of carbon nanomaterials to establish strong chemical bonds between each other[87]. For instance, Gatti et al. decorated PhOMe [p-methoxyphenyl] substituents to SWCNT and rGO, respectively[88], combined with P3HT in chlorobenzene dispersion to form 3 wt% SWCNT~PhOMe-P3HT and 4 wt% rGO~PhOMe-P3HT composites, promoting the formation of efficient charge percolation pathways. In the *second* way, functionalizing polymers helps to form a homogeneous mixing and facilitate a good interaction. Jung et al. employed PSSA

[poly(styrenesulfonic acid)] as a polymer template for solubilizing and stabilizing PANI in water[89], which they then mixed PSSA-PANI aqueous solution with GO dispersion to prepare graphene-PANI nanocomposite suspension, and was observed to be stable for several weeks without precipitation.

Solution blending is one of the most effective and simple methods to prepare homogeneous composites, and also easy to scale-up. Since it uses organic solvents to disperse carbon materials and polymers, the solution blending method requires drying process to remove solvents. Organic solvents may increase the cost of this method, and also possibly affect the composite performance if they are not removed completely[90].

3.2.2 In situ Polymerization

For *in situ* polymerization strategy (**Figure 2b**), carbon nanomaterials are mixed with the monomers (or pre-polymers) in a selective solvent, then the curing agent is added to initiate the polymerization reaction. Since monomers are used rather than polymers as the starting materials, *in situ* polymerization process leads to carbon-polymer nanocomposites with more uniform compositions and stronger interaction.

There are two approaches to initiate the polymer formation process: a chemical way or physical method. For example, in the *chemical* polymerization of PANI, an oxidative agent also as the curing agent is required. Ammonium persulfate [$(NH_4)_2S_2O_8$, APS] in HCl solution was dropwise added to the mixture of rGO and aniline [$C_6H_5NH_2$] in DI water, producing rGO-PANI composite[91]; potassium persulfate [$K_2S_2O_8$, KPS] also caused the polymerization of anilines along basal planes of rGO to form rGO-PANI nanocomposites[92]. In addition, a *physical* method (such as plasma treatment) can also initiate the polymer formation. Cogal et al. reported to use RF-plasma to prepare PEDOT/PTh-graphene composite, in which graphene powder was spread into plasma chamber and exposed to plasma produced by RF generator, meanwhile the monomer vapors flowed through the chamber, leading to the polymer formation on the surface of graphene nanosheets[93]. In this method, the polymer coating's thickness can be controlled by tuning the deposition time of RF-plasma.

The *in-situ* polymerization is great choice to deal with insoluble and unstable polymers. This technique also leads to a strong interaction between carbon materials and polymers. However, it is challenging to use this method to fully control the polymerization level and achieve high levels of exfoliation in large-scale production.

3.2.3 Melt Processing

In this method (**Figure 2c**), thermoplastic polymers are heated to a molten state, then mixed and blended with carbon nanomaterials, followed by the extrusion to produce the nanocomposites. The popular thermoplastic polymers include PP [polypropylene], PS [polystyrene], PC [polycarbonate], PEN [poly(ethylene-2,6-naphthalate)], etc.[94, 95] Shen et al. mixed PC and rGO in chloroform (C_6H_5Cl) solution, followed by stirring, sonication and centrifugation to collect the precipitation, then the dried composite was melt-mixed at 240 ^{0}C in a lab extrude to produce rGO-PC composites that contain PC wrapped on surface of rGO with noncovalent π- π stacking interaction[96]. The melt-mixing approach is more efficient than the traditional mixing for the dispersion of dry graphene nanoparticles in polymers[97].

Compared to the two previous methods, the melt processing is less versatile and more environmentally friendly to form carbon-polymer nanocomposites, thus is favorable for commercial production. But this method usually deals with thermoplastic polymers. And uniform dispersion of carbon materials is hindered due to high viscosity of thermoplastic polymers. Additionally, high temperature processing may also cause polymer degradation.

3.2.4 Coating

The coating method involves three different ways: (1) directly immersing the polymers into the solution of carbon nanomaterials; (2) layer-by-layer spin-coating of carbon film and polymer film, and (3) the mixed way (immersion and spin coating) (**Figure 2d**). In the direct immersion way, the porous structure of CNTs facilitated the infiltration of PEI [polyethylenimine], resulting in a uniform cross-stacked CNT-PEI composite[98]. Using the layer-by-layer strategy, GO solution in chlorobenzene and PMMA in chlorobenzene were each sequentially spin-coated on SWNT film, followed by drying and annealing to from a SWNT-GO-PMMA composite[99]. In addition, graphene-Ag nanowire (AgNW)-polymer hybrid composite was reported through the mixed immersion plus spin-coating way, whereas AgNW solution was firstly spin-coated onto the clean graphene-PTFE substrate, then the polymer in chloroform solution was coated onto the PTFE-graphene-AgNWs structure, followed by an annealing process to ensure an integral composite[100].

The coating methods such as spin-coating, spray-coating, roll-to-roll, and other coating techniques (lab- or large- scale) are feasible and practical to prepare carbon-polymer composite film. Although this method often requires following drying/sintering and pressing treatment, it is appropriate to produce thin films and coatings.

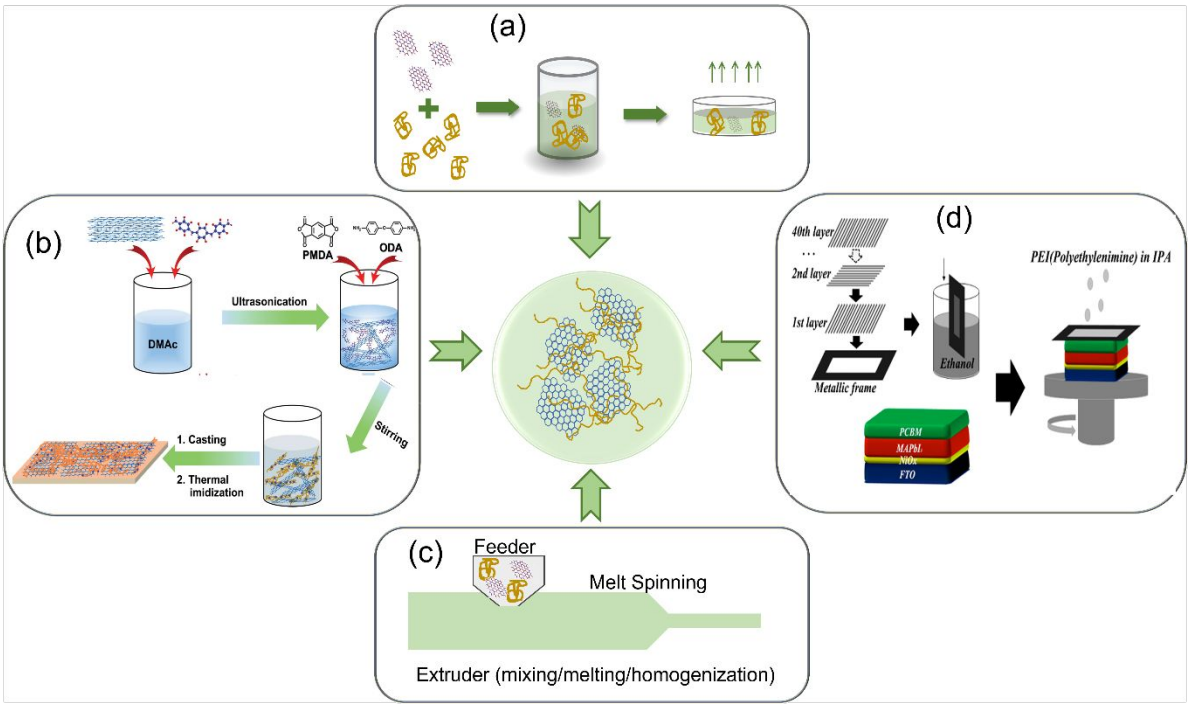

Figure 2 Preparation methods of carbon nanomaterials-polymer composites (a) Solution blending. (b) *in-situ* polymerization. Reproduced with permission.[101] Copyright 2017, Royal Society of Chemistry. (c) melt processing. Reproduced with permission.[102] Copyright 2020, Elsevier. (d) coating. Reproduced with permission.[98] Copyright 2018, American Chemical Society.

3.3 Physical and Chemical Properties of Polymer-Carbon Nanocomposites

The nanocomposites that contain both carbon material and polymer display impressive physical and chemical properties, including conductivity, thermal and mechanical properties[103].

3.3.1 Conductivity

High conductivity is important to achieve great photovoltaic properties of PSCs. Since carbon materials hold great electrical conductivity, adding them into polymers is expected to significantly improve their conductivity due to the formed electron transport networks[104]. For example, the rGO-PS composite displayed the electrical conductivity enhancement by five orders of magnitude upon increasing the rGO concentration from 0.25 vol.% to 2.5 vol.%[105]; GO-PANI composite also exhibited an improved conductivity of 10 S cm $^{-1}$ and specific capacitance of 531 F g^{-1} as compared to 2 S cm^{-1} and 216 F g^{-1} of pure PANI[106]. Mabrouk et al. compared the conductivity of three polymers (PEDOT:PSS, PANI, PANI-PEDOT:PSS) and their composite films with GO, and found that the PANI-PEDOT:PSS-GO composite exhibited

the highest conductivity of 0.814 S cm^{-1} owing to the synergistic effect and better interaction between each component[107].

Besides the electrical conductivity, the hole mobility of composite interlayers in PSCs was also improved. For instance, GO doped PEDOT:PSS HTL film showed the hole mobility of 1.57×10^{-4} $cm^2V^{-1}s^{-1}$, about one order of magnitude higher than its original value pristine PEDOT:PSS (5.55×10^{-5} $cm^2V^{-1}s^{-1}$)[51].

3.3.2 Thermal Properties

Improving thermal conductivity in PSCs can effectively reduce the thermal damage of perovskite and sprio-OMeTAD materials and thus improve the long-term stability. For polymer-carbon nanocomposites, the thermal conductivity is influenced by many factors, such as the compositions, the preparation technique as well as the geometry distribution of carbon material in the polymer matrix[108, 109]. For example, Yu et al. observed that the thermal conductivity of 25 vol% graphene-epoxy composite was 6.44 W/mK, which is ~30 times higher than that value of pristine epoxy (0.201 W/mK) [110]. More so, Guo et al. reported that the 25 wt% graphene- epoxy composite showed an improved thermal conductivity of 2.67 W/mK [111]. In another case, the thermal conductivity of 10 vol% multilayer graphene-epoxy nanocomposites displayed the increased thermal conductivity to 5.1 W/mK, which is 23 times higher than the initial value of epoxy [112].

A difference between inside temperature and ambient temperature of solar cell module can be as large as 45 °C when it is exposed to sunlight at 100 mW cm^{-2} irradiance[113]. Materials with good thermal conductivity and thermal stability are desired for solar cells. Giuri et al. used DSC and TGA to analyze thermal behavior of PEDOT:PSS-GO composite and found that thermal stability of polymer materials was enhanced when GO was added[86]. Besides, carbon-polymer composite also showed good thermal conductivity. Due to fast heat dissipation through thermally conductive rGO-PMMA composite, the thermal stability of PSC device with such composite film as the encapsulation layer was found to improve[84]. PCE of the device with rGO-PMMA coating was about 80% of initial value after 100h at 85 °C. While the efficiency of bare PSC and PMMA coated PSC decreased by 50% and 60% in 96 h at 85 °C. Thermal conductive rGO-PMMA coating minimized thermal damage of PSC devices.

3.3.3 Mechanical property

The carbon-polymer nanocomposites are also reported to show the enhancement on the mechanical properties (i.e. elastic modulus, friction coefficient, modulus, and flexibility) due

to the interface interlocking[114]. Qian et al. reported 1 wt.% MWNT-PS composites exhibited the elastic modulus of 1690 MPa and strength of 16 MPa, which were increased by 42% and ~25% in comparison with bare PS, respectively[115]. Zhao et al. loaded CNTs into hydroxyapatite composite and reported friction coefficient decrease as well as wear resistance increase[116]. For flexible optoelectronic devices, the graphene-polymer composites contribute to the mechanical robustness against repeated bending. Dong et al. prepared graphene-Ag nanowires-polymer composite and evaluated their flexibility by bending test with a radius of curvature of 2.0 mm [100]. After 250 cycles of tensile folding, the resistance only increased by 8% without any visible cracking or tearing on the surface.

4. Applications of Carbon-Polymer Nanocomposite in PSCs

Carbon nanomaterials such as graphene and carbon nanotubes are incorporated with polymers to form carbon-polymer nanocomposites. These materials have functioned as different roles in PSCs, including additives in perovskite layer, electrode, electron transporters, hole transporters, and barrier layer etc. The PSCs that contain carbon-polymer materials show enhanced performance including higher PCE values and long-term stability. In PSCs, the use of carbon-polymer materials contributes to one or more of the following aspects: (1) high quality perovskite films with high crystallinity and less defects; (2) improving conductivity to facilitate charge extraction and transportation; (3) adjustment on work function between different layers to achieve higher open circuit voltage; (4) great interface contact between layers to endow rapid carrier transport; (5) changing the hydrophobicity and thermal properties to prevent the attack from moisture and heat.

4.1 Additives in Perovskite Active Layer

In perovskite layer, carbon-polymer nanocomposites can play the following roles: (1) protective coating on surface of perovskite; and (2) additive in perovskite layer.

First, a protective coating on the perovskite surface is to prevent its degradation in working environments (air and humid). Rajamanickam et al. reported to deposit Graphene-PANI composite on the top of $CH_3NH_3PbI_3$ layer to protect it from degradation[117]. The morphology image (**Figure 3a and b**) showed that the perovskite crystals were fully encapsulated by the graphene-PANI composite rather than exposed to ambient conditions in the cases of graphene nanosheets- and PANI-only. The assembled PSCs were exposed for 96 h in extremely high humidity (99% RH), no perovskite degradation was observed. Moreover,

thick graphene-PANI composite coating (~4 μm) increased the tortuosity for the water molecules and oxygen diffusion into perovskite material. In addition, Ahn et al. designed a carbon-sandwiched PSC structure (**Figure 3c**, C_{60}/$MAPbI_3$/SWCNT), in which lead halide perovskite layer was sandwiched by C_{60} and SWCNTs without metal electrodes[118]. The PSC devices with three HTMs (spiro-MeOTAD, PTAA and P3HT) infiltrated in SWCNTs gave average PCE of 17.0 %, 15.3% and 13.6%, respectively. The supramolecular CNT-polymer hybrids were formed by inducing π-π interactions between polymers and CNTs[119], in specific, P3HT led to a much better stability than that of PTAA due to its planar conformation which leaded to a close interaction with CNTs by wrapping around nanotubes.

Second, additives to influence the crystallization and growth of perovskites, or reduce defects in perovskite materials during operation. Sarvari et al. grafted reduced graphene oxide with P3HT (or PTEt), and added the rGO-P3HT composite (or rGO-PTEt) into the perovskite precursor solution[120]. The composite additives effectively enhanced the grain size and increased the crystallinity (**Figure 3d and e**), thus improved the absorbance efficiency of pristine perovskite due to grafting of rGO surface with the polymeric backbones. The P3HT-rGO-based PSC device showed a PCE of 15.15% with V_{oc} of 0.95 V, J_{sc} of 22.15 mA cm^{-2}, and an FF of 72%. In addition, for working PSC devices, some harmful defects (i.e. local positive and negative ion vacancies) are formed as the cation and halogen ions of perovskite migrate under the internal electric field of the device[121, 122]. Recently, Lou et al. added the graphene-polymer (e.g. PM6, PM7 Lewis base conductive polymer) nanocomposite during the antisolvent step of Cs/FA/MA [$Cs_{0.05}FA_{0.79}MA_{0.16}PbI_{2.49}Br_{0.51}$][123]. The highly conductive graphene-polymer composites not only passivated the defects dominated by state traps, but also facilitated the charge transport in perovskite film, which reduced the interfacial charge density and trap-assisted charge recombination. The PSCs with graphene-PM6 composite additive showed a high PCE of 21.21% (Figure 3f) with V_{oc} of 1.17 V, J_{sc} of 24.03 mA cm^{-2}, and an FF of 76%, in compared to PCE (18.21%) of the control device without composite. Moreover, due to the hydrophobicity of polymer-graphene composite, the graphene-PM6 and graphene-PM7-based devices showed outstanding stability by maintaining 90% and 85% of the initial PCE after 480 h aging under ~35% RH at room temperature, respectively.

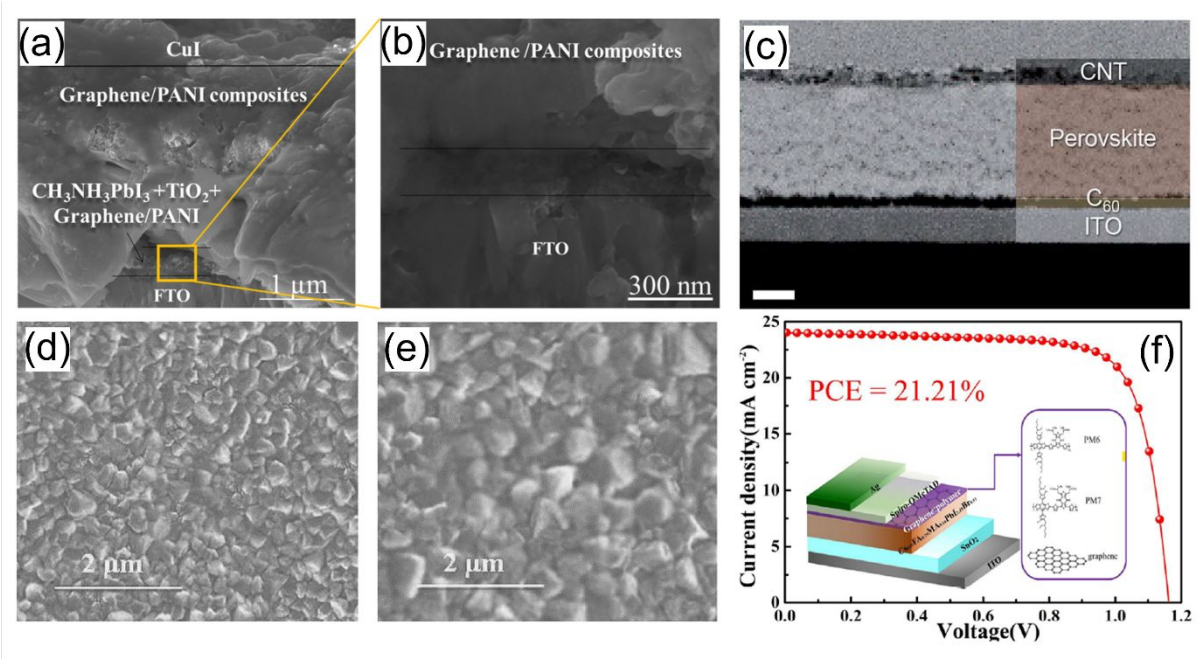

Figure 3 (a) and (b) Cross-sectional scanning electron microscopy image of graphene/PANI protected $CH_3NH_3PbI_3$ solar cell. Reproduced with permission.[117] Copyright 2016, Institute of Physics Publishing. (c) Cross-sectional SEM images of the ITO/C_{60}/$MAPbI_3$/CNT device with carbon-sandwich structure. Reproduced with permission.[118] Copyright 2018, Royal Society of Chemistry. (d) FSEM images of $CH_3NH_3PbI_3$ (e) FSEM images of perovskite + rGO-P3HT. Reproduced with permission.[120] Copyright 2019, Elsevier; (f) Device architecture and *J*−*V* curve for best devices of PSCs based on graphene/PM6. Reproduced with permission.[123] Copyright 2021, American Chemical Society.

4.2 Electrode

4.2.1 Transparent Electrode

Carbon-polymer thin films, with good flexibility and transparency, have shown promises as the transparent electrode for solar cells. Dong et al. employed up-bottom preparation to produce a flat hybrid electrode of graphene-Ag nanowire-polymer (MG-A-P), which exhibited better optical-electrical properties (sheet resistance 8.06 Ω/□ and 88.3% optical transmittance at 550 nm in **Figure 4a and b**) than the traditional transparent electrode such as ITO[100]. Moreover, the resistance of MG-A-P hybrid film increased 8% after 250 cycles of bending test with a radius of curvature of 2.0 mm while ITO-PET film rapidly cracked, and the resistance remarkably increased after 5 cycles of bending test. The enhanced properties are resulted from the hybrid structure, in which the polymer matrix entirely wrapped the conductive components (graphene and Ag wire). Due to the excellent mechanical properties, carbon-polymer based materials

possess tremendous potential in application for flexible PSCs that with features of high efficiency, low cost and lightweight[124]. However, as the transparent electrode, carbon-polymer thin films need to balance the conductivity and light transparency. Higher carbon content in the composite results in higher conductivity but leads to poor light transparency.

4.2.2 Back Electrode

Metallic materials such as gold and silver which have high conductivity are typically used back electrodes in PSCs. However, their high temperature vacuum evaporation deposition increase the fabrication cost[125]. The migration of metals to perovskite layer severely compromise the long-term stability of devices[20, 126]. Carbon-polymer nanocomposites are demonstrated as great candidates to replace metal electrode because of their low cost, flexibility, good conductivity and chemical inertness. You et al. reported semitransparent PSC devices that utilize graphene-PMMA-PDMS [polydimethylsiloxane] film with PEDOT:PSS spin-coated on the graphene surface (**Figure 4c**)[58]. The PEDOT:PSS layer introduced more holes in the graphene film and improved the conductivity, with sheet resistance decreased from 1050 Ω sq $^{-1}$ to 260 Ω sq $^{-1}$. The obtained PSC devices were with transparency of 50% for 150 nm thick perovskite layer (**Figure 4d**). Thus, the PSC devices showed an average PCE up to 12.02 % and 11.65% from bottom (FTO side) and top (graphene side) electrodes illumination, respectively. In addition, Zhou et al. demonstrated a cross-stacked carbon nanotube (CSCNT)-PEI (0.5 wt%) composite electrode for inverted PSCs[98]. The presence of PEI promoted a better interface contact and charge transfer between HTL (PCBM) and CSCNT electrode, also tuned the work function of the electrode in the inverted PSC (**Figure 4e**), yielding to the PCE of ~11% for the assembled PSCs. Moreover, since CSCNT-PEI electrode was thermotolerant without metal-ion diffusion and accumulation, the resulted PSCs showed increase in stability, in specific, they retained over 94% of original efficiencies after 500 h storage in ambient air and 90% after 500 h thermal treatment at 60 °C (**Figure 4f**). Similarly, Zheng et al. developed mesoscopic PSCs using P3HT modified CNTs (CNTs@P3HT) as the counter electrode [85]. In the P3HT-CNT composite, P3HT not only tightly bound the CNTs together to form a cross-linked structure to improve the interaction with perovskite layer and endow rapid carrier transport, but also extracted holes to facilitate carrier separation due to its hole-transporting property.

Carbon-polymer composites, as the back electrode candidates, show advantages of (1) easy to process to thin films with tunable thickness and component as well as properties; (2) low cost and hold excellent mechanical properties; and (3) great stability towards to perovskite

structure. However, the conductivity of composite is relatively lower than metal electrode especially when insulating polymers are added. Thus, the combination of metal and transparent conductive oxide electrodes leads to high efficiency of PSC devices.

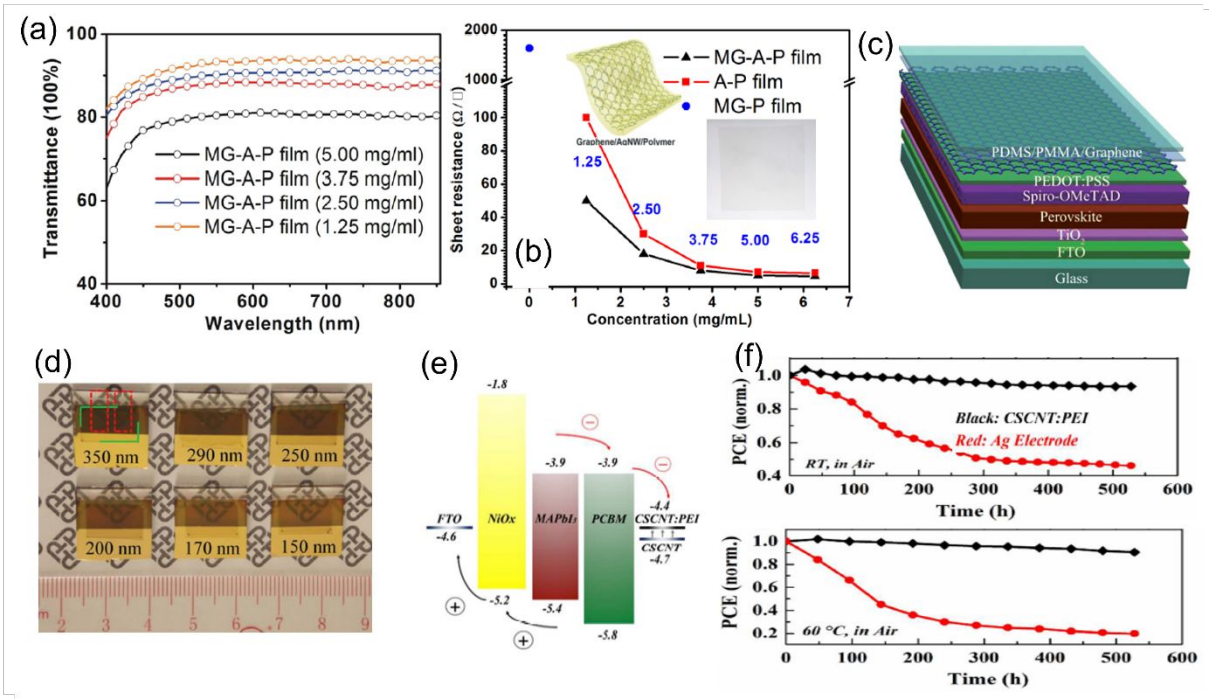

Figure 4 (a) Optical transmittance spectra of graphene−AgNWs−polymer (MG-A-P) film with various concentrations of AgNWs, (b) Sheet resistance of the MG-P, MG-A-P, and A-P hybrid films with different concentrations of AgNWs. Reproduced with permission.[100] Copyright 2016, American Chemical Society. (c) Schematic diagram of a semitransparent perovskite solar cell using graphene as counter electrode, (d) Photos of semitransparent perovskite solar cells with transparent graphene electrodes. The thicknesses of the perovskite layers in the six devices are approximately 350, 290, 200, 170, and 150 nm, respectively. Reproduced with permission.[58] Copyright 2015, Wiley-VCH. (e) Schematic energy level diagram of FTO/NiO_x/$MAPbI_3$/PCBM/CSCNT:PEI device, (f) the variation of PCE of Ag and CSCNT:PEI based PSCs as a function of ageing time at room temperature (RH: 10%-50%, T: 20-30 °C) and with a constant temperature of 60 °C. Reproduced with permission.[98] Copyright 2018, American Chemical Society.

4.3 Encapsulation layer

CNMs-polymer composite coatings also function as a barrier layer, which significantly increases the long-term stability of PSCs in humid and hot environments. Han et al. deposited

a PMMA-rGO composite (PRC) passivation layer on the top surface of PSCs (**Figure 5a**)[84]. The rGO nanosheets with hydroxyl group and amphiphilic PMMA molecules with carbonyl group contributed the hydrophobic nature (**Figure 5b**) and better thermal conductivity PMMA-rGO composite coating, improving the photovoltaic stability under humid environment and high-temperature conditions. With the PMMA-rGO passivation layer, the PSC devices displayed slight decrease of 10% on the PCE after exposure to very humid conduction (RH>75%) for 500 hours. When exposed to 90°C for 100 hours, the PCE of PSC devices with passivation layer was maintained at 12.6%, which is about 80% of the initial value (**Figure 5c**). Jang et al. reported the encapsulation layer consist of GO and SiO_2 fillers in EVOH [poly(vinyl alcohol-co-ethylene)] matrix (**Figure 5d**)[127]. SiO_2 nanoparticles (5 wt%) were added into EVOH to reduce the permeation of oxygen and water; and introducing 1 wt% GO into EVOH/SiO_2 further decreased the water vapor transmission rate (WVTR). The EVOH-GO-SiO_2 encapsulation layer did not damage the efficiency of PSC devices, whereas the PCE of 17.86% with and 17.28% without the layer (**Figure 5e**). Moreover, with the composite protective layer, the PSCs devices remained approximately 86% and 61% of the initial PCEs after 5 and 10 h from the onset of the reservoir test (direct contact with water on the encapsulated surface). In comparison, the unencapsulated device was immediately degraded after contacting with water (**Figure 5f**). **Table 2** summaries the device configurations and PV performances for PSCs using carbon-polymer composite as additives, electrode and encapsulation layer.

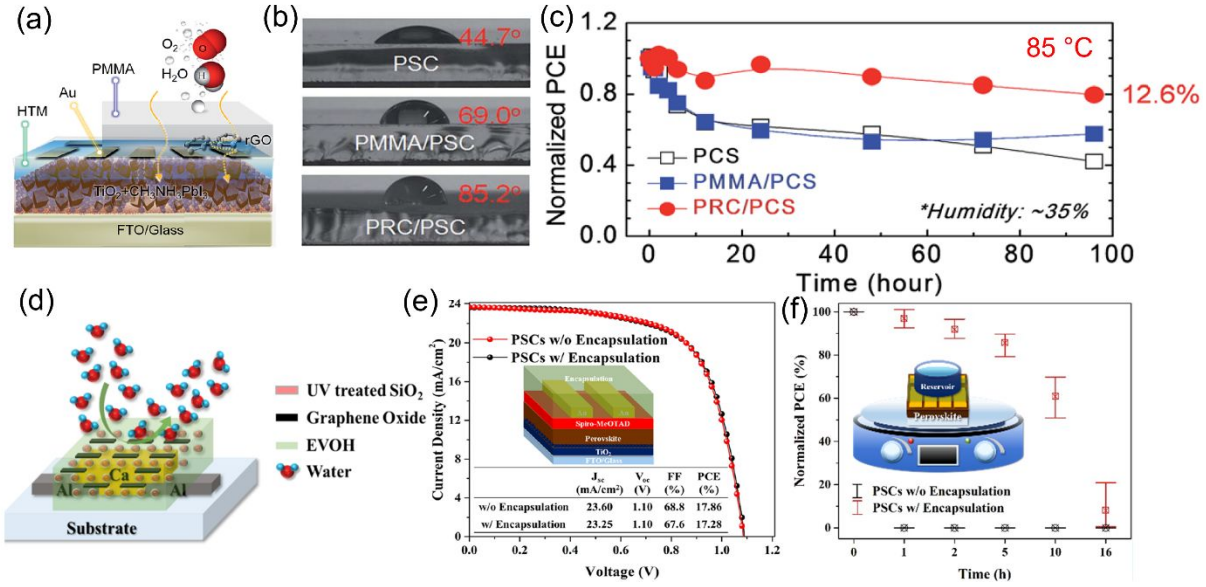

Figure 5 (a) Schematic representation of the hydrophobic surface and external matter following a complex path through PRC layer, (b) water contact angles of bare cells, PMMA/PSC and PRC/PSC on the top, (c) Change in PCE of PSCs at 85 ^{0}C for 96 h (normalized using PCEs of as-fabricated cells. Reproduced with permission.[84] Copyright 2017, Royal Society of Chemistry. (d) Scheme of PSCs encapsulated with EVOH/S5/UV/G1, (e) Efficiency of PSCs before and after encapsulation, (f) Reservoir test of PSCs encapsulated with EVOH/S5/UV/G1. Reproduced with permission.[127] Copyright 2019, American Chemical Society.

4.4 Charge transport layer

Carbon nanomaterials-polymer composites are proven to be good candidates for both ETL and HTL materials in PSC structure. In the composite, the combination of polymer (amorphous nature and strong intrachain charge transfer along the conjugated backbone) and carbon nanomaterials with great conductivity endows their good balance between high film quality and charge mobility.

4.4.1 Electron Transport Layer (ETL)

PANI is a popular polymer that has been widely used together with carbon nanomaterials in ETL[128, 129]. The carbon-PANI nanocomposite can either serve as a promising ETL material or function as an additive.

In 2016, Tong et al. demonstrated the use of mesoporous graphene-PANI (mp-GP) as a ETL candidate in PSC devices (**Figure 6a**) with good thermal stability [92]. The network structure of mp-GP composite contains pores (100-400 nm), which not only to form a well-connected serve as fast electronic channels but also allow for larger perovskite crystals (**Figure 6b and**

c). The resulted mp-GP based PSC device displayed remarkable PCE of 13.8% in comparation to that of 9.3% with rGO based device. Regarding the stability, it is known that the basicity of ETL materials (e.g. ZnO) is one driving force for the thermal decomposition of perovskite[130]. Mp-GP with low isoelectric point strengthened the stability of perovskite better against thermal decomposition. Moreover, the mesoporous architecture protected the inner perovskite grains from moisture attack and reactive interface formation. For mp-GP based devices, their PCE retained ~88% of initial efficiency after 200 h thermal annealing at 150 ^{0}C. This mesoporous graphene-polymer composite served as a promising ETL material.

Recently, Mohseni et al. added rGO-PANI nanocomposite as an additive to typical mesoporous TiO_2 (mp-TiO_2) ETL precursor in mesoscopic-type PSCs, leading to the reduction in surface defects and passivated grain boundaries of the upper perovskite layer[91]. Furthermore, the incorporation of rGO-PANI nanocomposite strengthened the charge transfer in the ETL layer as well as the interface with perovskite. The 4 vol% rGO-PANI-based device achieved the highest PCE of 16.48 % (**Figure 6d**) and also displayed enhanced stability, whereas 82% of initial PCE was maintained over 1870 h of aging time inside a dry airbox at a temperature of 20-30 ^{0}C (**Figure 6e**). In contrast, the PCE of rGO-based device declined to 15% of its original value.

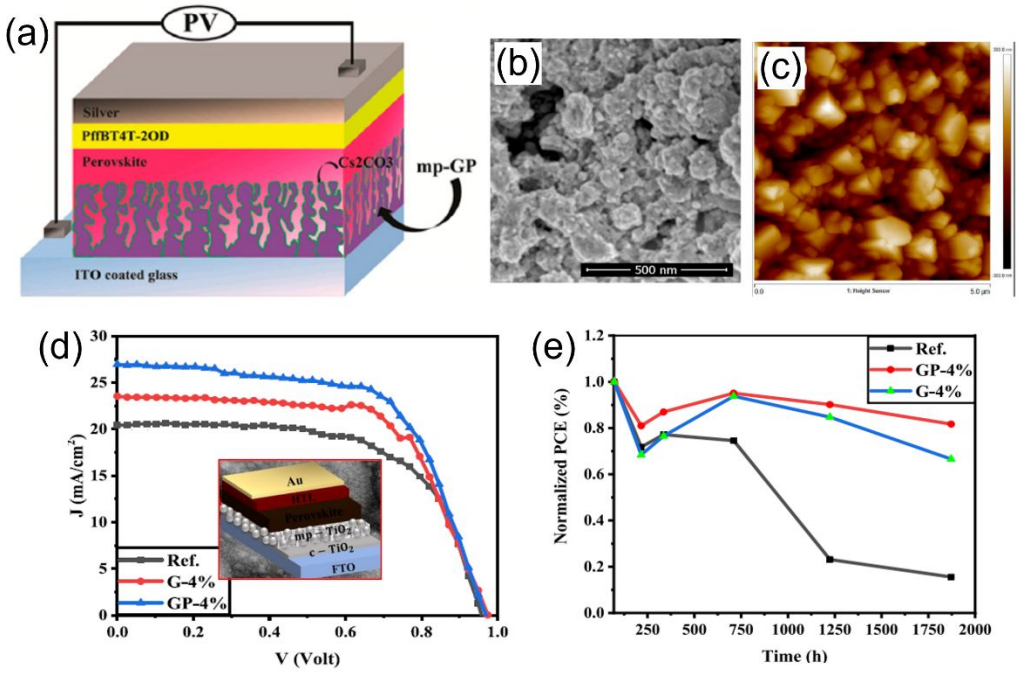

Figure 6 (a) Schematic view of the device structure with ITO/mp−GP or rGO/Cs_2CO_3/$CH_3NH_3PbI_3$/PffBT4T-2OD/Ag, (b) SEM image and (c) AFM image of topography of the mp−GP thin films. Reproduced with permission.[92] Copyright 2016,

American Chemical Society. (d) The *J-V* of the perovskite solar cells (PSCs) fabricated based on pure mp-TiO_2 and the mp-TiO_2 ETL modified with rGO-PANI nanocomposite or pure rGO, (e) stability test of different perovskite solar cells inside a dry airbox with the relative humidity of about 20% in dark at room temperature. Reproduced with permission.[91] Copyright 2021, Elsevier.

4.4.2 Hole Transport Layer (HTL)

Typically, PSC devices contain organic spiro-OMeTAD as HTL material. Alternative materials include PEDOT:PSS and P3HT. PEDOT:PSS is a popular polymer that combines with graphene and related materials (GO and rGO) to form composites. The work function of PEDOT-DOT is 5.08 eV, which well-match with graphene oxide (4.9 eV) and results in more efficient charge transport and collection to electrode[131].

To take advantage of the high conductivity and hydrophobicity of pristine graphene, nanocomposites of graphene-polymers have been explored using various polymers such as PEDOT, PEDOT:PSS, P3HT. In 2018, Cogal et al. reported to prepare nanocomposites of graphene with PTh [polythiophene] or PEDOT prepared using radio frequency (RF) plasma polymerization[93]. They found that the PSC devices with I_2 doped PEDOT-graphene showed higher PCE (8.79%) than I_2 doped PTh-graphene (4.95%). Later, Redondo-Obispo et al. reported to incorporate few-layer graphene platelets into PEDOT:PSS (**Figure 7a**) to form HTL composite, which influenced the subsequent growth of perovskite layer (i.e. inhibited the formation of PbI_2 and decreased grain boundary density)[132]. The G-doped PEDOT:PSS composite also exhibited better charge extraction and reduction of recombination at the interface between composite HTL and perovskite. The PSC device with 0.02 mg/mL G-doped PEDOT:PSS HTL displayed the highest PCE (**Figure 7b**). In 2019, Chu et al. developed P3HT-graphene composite to replace pure P3HT as HTL material in PSC devices (**Figure 7c**)[133]. The graphene-P3HT composite exhibited outstanding hole mobility of 1.2 $\times 10^{-2}$ $cm^2V^{-1}s^{-1}$, two orders of magnitude lager than pure P3HT. The carbon-based PSC with graphene-P3HT composite achieved a high PCE of 18.1% in comparison to 11.1% of pure P3HT-based PSC. Impressively, the devices with graphene-P3HT composite HTL showed long-term stability, which revealed by 97% remained PCE after storage for 1680 hours under ambient conditions (RH 50%) without illumination (**Figure 7d**). In addition to pristine graphene, functional graphene (F-graphene)-modified P3HT composite had been prepared by Ye et al. and employed as HTL in PSC devices. The high conductivity of F-graphene enhanced the hole mobility of

composite HTL and modified the energy level of the device (**Figure 7e**)[134]. Using 4 wt% F-graphene in P3HT layer, the PSCs with composite HTL showed the highest EQE value and IPCE value (**Figure 7f**), consistent with the highest PCE of 13.82%.

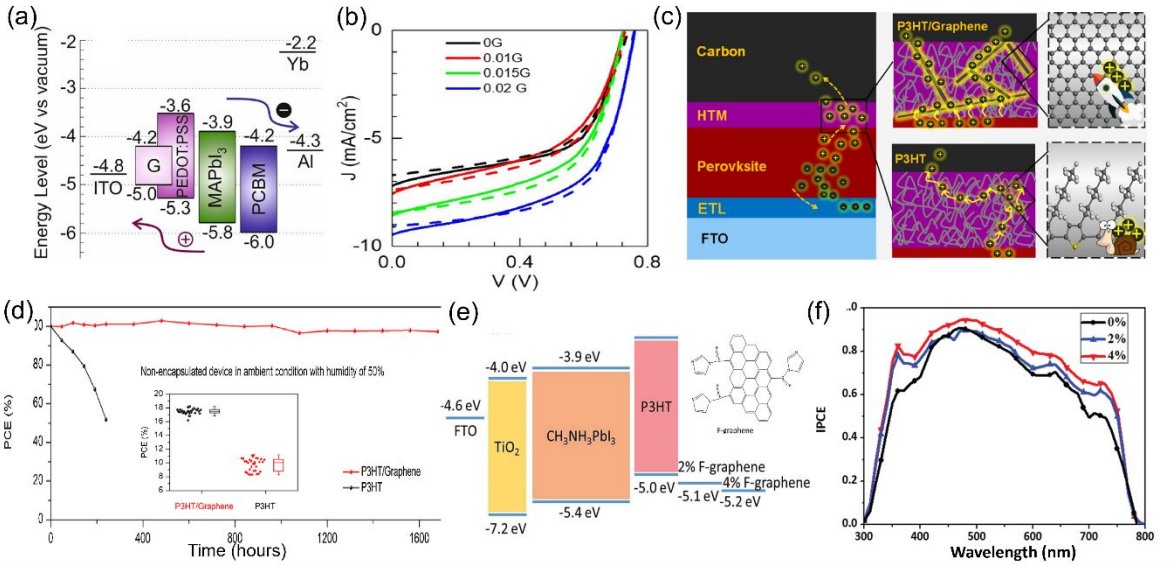

Figure 7 (a) Energy level diagram for PSC with graphene-doped PEDOT:PSS as HTL materials, (b) current-voltage performances under 1 sun illumination for the solar cells based on 0G, 0.005G, 0.01G, 0.015G and 0.02G as HTL in forward sweep (solid lines) and reverse sweep (dashed lines). Reproduced with permission.[132] Copyright 2020, Elsevier. (c) Illustration of device with P3HT as the HTL, where the hole transport is slow, resulting in charge accumulation, and device with P3HT-graphene composites HTL, where hole transports to the carbon electrode quickly, (d) Normalized PCE evolution of non-encapsulated devices with P3HT and graphene-P3HT as the HTLs stored in the dark for 1680 h in air, insert is the statistical PCEs of devices with graphene-P3HT and P3HT as HTL. Reproduced with permission.[133] Copyright 2019, Elsevier. (e) The schematic energy diagram of the hole-transporting layer involved in the PSCs, (f) The corresponding external quantum efficiency (EQE) spectra of the PSCs devices with various HTMs. Reproduced with permission.[134] Copyright 2016, Royal Society of Chemistry.

Graphene oxide (GO) has been used to form composites with polymers including PEDOT:PSS, PEDOT, and PANI. In 2016, Lee et al. investigated GO-PEDOT:PSS composite as HTL for planar PSCs, and they observed higher photovoltaic performance of PSCs with composite HTL (9.74%) than those of pristine PEDOT:PSS (8.23%) and GO (6.42%) HTL[131].

The enhanced performance is attributed to more efficient hole transport and collection. In 2018, Yu et al. fabricated inverted PSCs through solution-mixing method to prepare GO-PEDOT:PSS composite as HTL[135]. The GO-PEDOT:PSS (volume ratio of 2 to 1) composite showed the better matched HOMO level (5.42 eV) with that of perovskite layer (5.4 eV) than pristine PEDOT:PSS (5.08 eV)(**Figure 8a**), improving the hole extraction. The inverted PSC with composite HTL displayed a PCE of 18.09%, higher than that of PSC with pristine PEDOT:PSS (14.95%). The steady-state and time-resolved photoluminescence (PL) spectra (**Figure 8b**) also confirmed that the PL intensity of the perovskite film prepared on the PEDOT:GO composite decreased about 97%, along with a remarkable decreasing exciton lifetime. In the GO-PEDOT:PSS composite HTL, Niu et al. studied the influence of different concentrations of GO on the photostatic performance of PSC devices[51]. The GO doping to PEDOT:PSS reduced the root mean square (RMS) roughness value (**Figure 8c**) and provided high quality surface for perovskite deposition. They observed the PSC with PEDOT:PSS+500μL GO showed the highest J_{sc} value (20 mA/cm^2) and PCE (14.2%) since the oversaturated GO in composites caused the segregation and barriers between GO and PEDOT:PSS as well as poor conductivity. In addition, Mabrouk et al. compared five different HTL materials for p-i-n PSCs: pristine GO, PEDOT:PSS, PEDOT:PSS-PANI (2/1), GO-PANI (2/1), and PANI-PEDOT:PSS-GO (1:1:1) (**Figure 8d**)[107]. When using the GO-PEDOT:PSS-PANI (ratio of 1:1:1) composite as HTL, the PSC device achieved the highest efficiency of 18.12%. The enhanced J_{sc} value was attributed to the higher conductivity and well-matched energy levels (**Figure 8e**), meanwhile, the improved V_{oc} was resulted from the increase of work function after adding GO to PEDOT:PSS-PANI. The surface chemistry of GO can be functionalized with atomic groups and form composite with polymers. Guo et al. prepared sulfated graphene oxide (sGO) with -SO_3H groups and combined it with PEDOT:PSS to form composites as HTL for PSCs[136]. They found that sGO as HTL showed better device efficiencies (max. PCE 9.9%) than GO HTL (max. PCE 6.7%). Moreover, the 1:1 sGO-PEDOT composite HTL based device achieved the best PCE of 13.9% and less photocurrent hysteresis due to the most efficient charge carries generation and transfer.

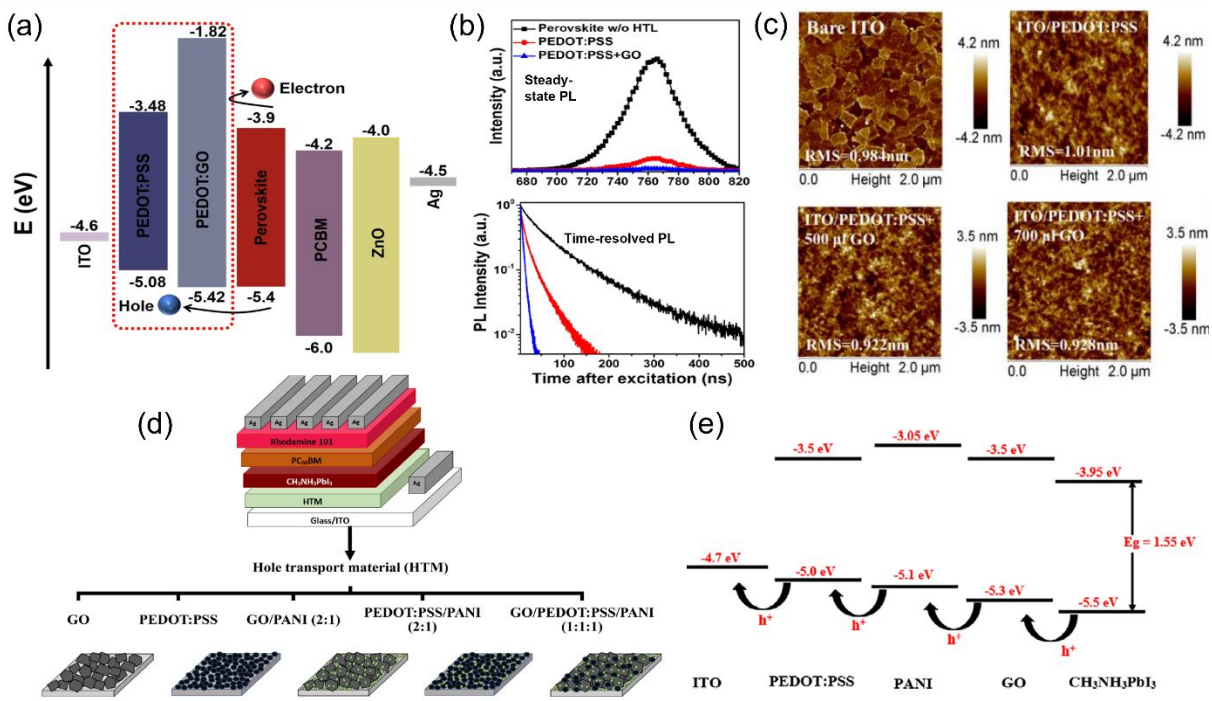

Figure 8 (a) Relative energy levels of the various device components in the perovskite solar cells, (b) steady-state PL spectra and time-resolved PL spectra of perovskite films prepared on PEDOT:PSS and GO-PEDOT:PSS composites, respectively. Reproduced with permission.[135] Copyright 2018, Springer Nature. (c) AFM images of GO-doped PEDOT:PSS films spin-coated on ITO glass using different concentration. Reproduced with permission.[51] Copyright 2017, Elsevier. (d) Structure of p-i-n perovskite solar cells using different HTMs: GO, PEDOT:PSS, GO-PANI, PEDOT:PSS-PANI, and GO-PEDOT:PSS-PANI nanocomposites, (e) Schematic diagram showing energy levels of ITO, $CH_3NH_3PbI_3$ perovskite and different HTMs, including PEDOT: PSS, PANI, and GO. Reproduced with permission.[107] Copyright 2020, Wiley-VCH.

Reduced graphene oxide (rGO) as another 2D graphene derivative has been explored to prepare carbon-polymer composites for HTL materials. Jung et al. prepared rGO-PANI nanocomposite films and demonstrated them as HTL materials in the inverted PSCs[89]. The rGO-PANI based device achieved a PCE of 16.61%, higher than that of PSCs with GO-PANI as HTL (14.1%) (**Figure 9a**). The enhanced photostatic performance was attributed to the higher conductivity and better energy level matching to the perovskite layer with rGO-PANI nanocomposite (**Figure 9b**). Recently, Cho et al. used electron-beam to reduce GO-PVP composite in aqueous ethanol solution and prepared highly dispersible rGO-PVP nanocomposite[137]. PVP acted as stabilizer to impede the re-aggregation during the reduction

process of GO. When used as HTL in PSCs, the aggregation-free rGO-PVP nanocomposite showed the highest PCE of 11.36% (**Figure 9c**) and more efficient photon-to-electron conversion than other HTL materials (GO, PVP, PEDOT:PSS) (**Figure 9d**). To obtain better dispersion in polymer, Cho et al. employed high energy ^{60}Co γ-ray irradiation to produce smaller GO sheets (**Figure 9e**) and uniform distribution of γ-ray irradiated GO in PEDOT:PSS [138]. The better dispersion resulted in more efficient hole charge transport between GO and PEDOT:PSS in HTL. The γ-ray-GO embedded PEDOT:PSS interlayer assisted to improve the crystallinity of perovskite layer, resulting in the higher photovoltaic performance with PCE of 12.76% than the devices without GO or with pristine GO (**Figure 9f**). Moreover, the photoluminescence spectra (**Figure 9g**) also confirmed the best charge separation in the PSCs with γ-ray-GO-PEDOT:PSS composite.

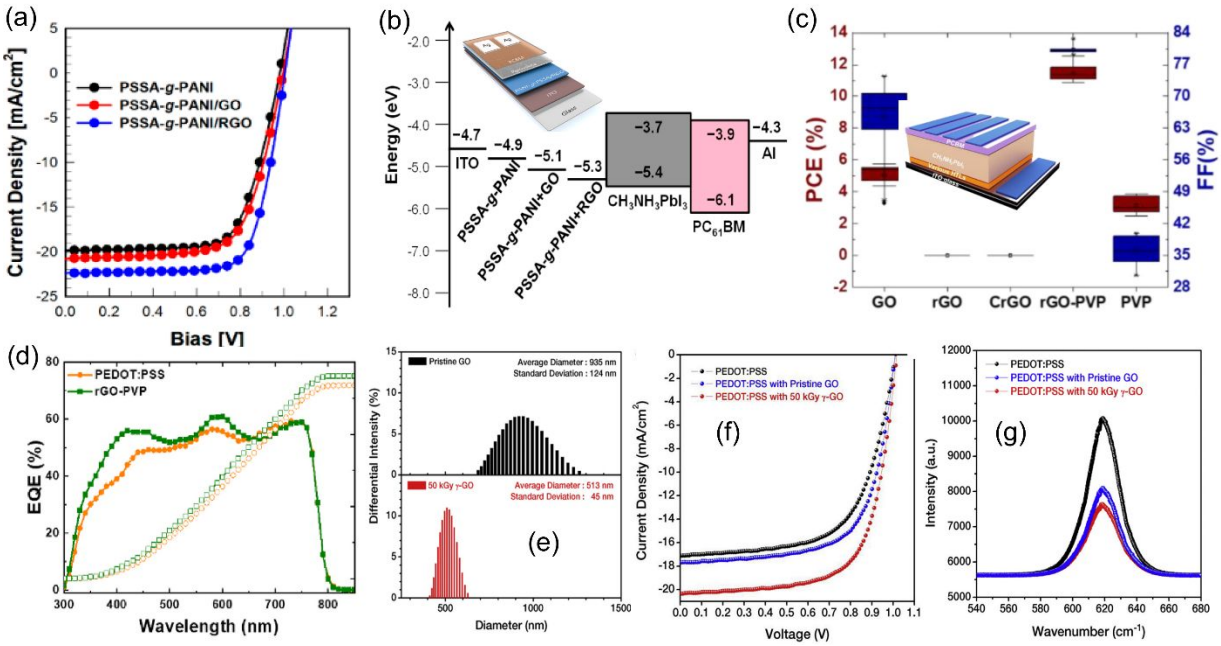

Figure 9 (a) *J-V* curves of PSCs with PANI, GO-PANI, and rGO-PANI as HTLs under 1-sun illumination, (b) Energies levels of composite films in PSCs (insert is Schematic device structure). Reproduced with permission.[89] Copyright 2021, Multidisciplinary Digital Publishing Institute. (c) Statistical data of PCE and FF of PSCs with various HTLs, (insert is schematic of rGO-PVP-based PSC device structure), (d) EQEs with integrated J_{sc} of PSCs using PEDOT:PSS and rGO-PVP as HTL. Reproduced with permission.[137] Copyright 2021, Elsevier. (e) Size distributions of pristine GO and 50 kGy γ-ray-GO dispersed in water measured by DLS measurements, (f) *J-V* curves and EQE spectra of the cells with PEDOT:PSS, PEDOT:PSS with pristine GO, and PEDOT:PSS with 50 kGy γ-ray-GO as hole transport layer, (g)

Photoluminescence spectra of perovskite layers on PEDOT:PSS layer, PEDOT:PSS with GO, and with 50 kGy γ-ray-GO. Reproduced with permission.[138] Copyright 2018, Elsevier.

Carbon dots usually have various functional groups such as carbonyl, hydroxyl, and epoxy groups[82]. The interaction between carbon dots and PEDOT:PSS can enhance the conductivity of the composite. Li et al. incorporated graphene quantum dots (GQDs) into PEDOT:PSS and used this composite film as HTL[139]. They found that GQDs increased the conductivity of composite film because graphene quantum dots interacted with PEDOT:PSS chain, leading to a phase separation. The average PCE was boosted from 12.77% for PEDOT:PSS based PSCs to 15.24% for PEDOT:PSS-GQDs based devices. Li et al. developed S, C co-doped carbon nanodots (CNDs)-PEDOT:PSS composite HTL for inverted PSC[140]. Sulfur double bond of functionalized CNDs banded the superfluous PSS and removed the insulating component from PEDOT:PSS mixture, resulting in conductivity and hole extraction capability enhancement. Meanwhile, the amidogen on the surface of functionalized CNDs neutralized hydrogen ions from PSS sour and lowered the level of acidity of PEDOT:PSS. The optimized PSCs demonstrated a promising air stability and photovoltaic performance including V_{oc} of 1.01 V, J_{sc} of 22.6 mA cm^{-2}, and a FF 79.06%, yielding a PCE of 18.03%.

Polymer-functionalized single wall carbon nanotubes (SWNTs) have been employed to work as HTL material. In 2014, Habisreutinger et al. wrapped P3HT with SWNT to form a supramolecular nanohybrids film by spin-coating, and combined with insulating PMMA to prepare meso-superstructured PSCs (**Figure 10a**)[17]. The P3HT-SWNT-PMMA based PSCs displayed the maximum PCE of 15.3% and impressive thermal stability, where the average scanned PCE before and after thermal stressing at 80 ^{0}C for 96 h changed from 11.1 to 10.1%. In addition, the PSCs device on SWNT-P3HT-PC showed improved thermal stability at temperature above 80 ^{0}C (**Figure 10b**) as well as moisture stability by the comparison of an unsealed device before and after exposure to running water (**Figure 10c**). The composite of functionalized SWNTs within inert polymer matrix achieved competitive efficiency and offered resilience against thermal and moisture stressing. The authors also deposited spiro-OMeTAD on the P3HT-SWNTs layer[141]. Spiro-OMeTAD filled the opening and gaps of nanotube layer, which facilitated an efficient charge transfer. The device with a stratified structure of P3HT-SWNT and Spiro-OMeTAD yielded a PCE of 15.4%. In 2017, Habisreutinger et al. further demonstrated a PCE of 18.8% for the device with a double-layer structure of P3HT-SWNT and spiro-OMeTAD as hole-transporting p-type layer and $FA_{0.83}MA_{0.17}Pb(I_{0.87}Br_{0.17})_3$ as absorber[142]. Besides, Wang et al. reported that using a SWNT-GO-PMMA thin film as a hole

conductive protecting layer in PSCs[99]. In the composite, GO acts as an electron-blocking layer while SWNT functions as an efficient carrier dissociation and hole extraction layer in the band alignment (**Figure 10d**). Combing with PMMA layer as an effective barrier, high photovoltaic performance stability was achieved for SWNT-GO-PMMA based PSCs, where the PCE changed from 10.5% to 10% after 10 days, compared with that of spiro-OMeTAD based PSC dropped from 10.5% to 5.8%. The PSC with SWNT-GO-PMMA as HTL showed the high PCE of 13.3% (**Figure 10e**). When P3HT was in conjunction with MWCNTs and used as HTL in $CsPbI_2Br$ PSC, Wang et al. demonstrated that a conversion efficiency of 10.01% was achieved due to the enhanced holes extraction and transport[143]. MWCNTs-P3HT composites also prevented moisture ingress, ~85% initial PCE was retained over 240 h under ambient conditions.

For the composite HTL materials, the prevention of CNMs aggregation in polymer matrix is a key issue to create well-separated pathways for charge percolation in a specific direction at the nanoscale level. Thus, functionalization of the carbon nanomaterials with organic groups is a useful way to facilitate their homogeneous dispersion in polymer matrix. In 2016, Gatti et al. reported P3HT [poly(3-hexylthiophene)] matrix doped with organic functionalized SWCNTs and rGO as HTL in PSC devices[88]. To facilitate the dispersion of SWCNT and rGO in P3HT polymer matrix, p-methoxyphenyl substituents were introduced to form composite HTLs (**Figure 10f**). Using 2 wt% SWCNT-PhOMe-P3HT and 4 wt% rGO-PhOMe-P3HT composite, the best PCEs of 11.6% and 10% for planar PSCs were achieved, PCEs of 11% and 7.3% were left after 480h endurance test, respectively (**Figure 10g and h**). Moreover, after the endurance tests of over 3240h, SWNTs- and rGO- doped PSCs showed average PCE of 8.7% and 4.7% compared to the devices based on the un-doped polymer (PCE=0). The increase in photovoltaic performances and stabilities were attributed to the improved interfacial contacts between the HTL and adjunct layers. In 2018, Gatti et al. further investigated five different substituents bond (thienyl-type and alkyl-type) to rGO flakes on the morphology and structure of functionalized rGO-P3HT HTLs (**Figure 10i**)[144]. They demonstrated that the morphology of dispersed rGO flakes in a P3HT thin film could be tuned by tailoring the intermolecular interactions between two constituents in the composite. **Table 3** summaries the device configurations and PV performances for PSCs using carbon-polymer composite as charge transport layer.

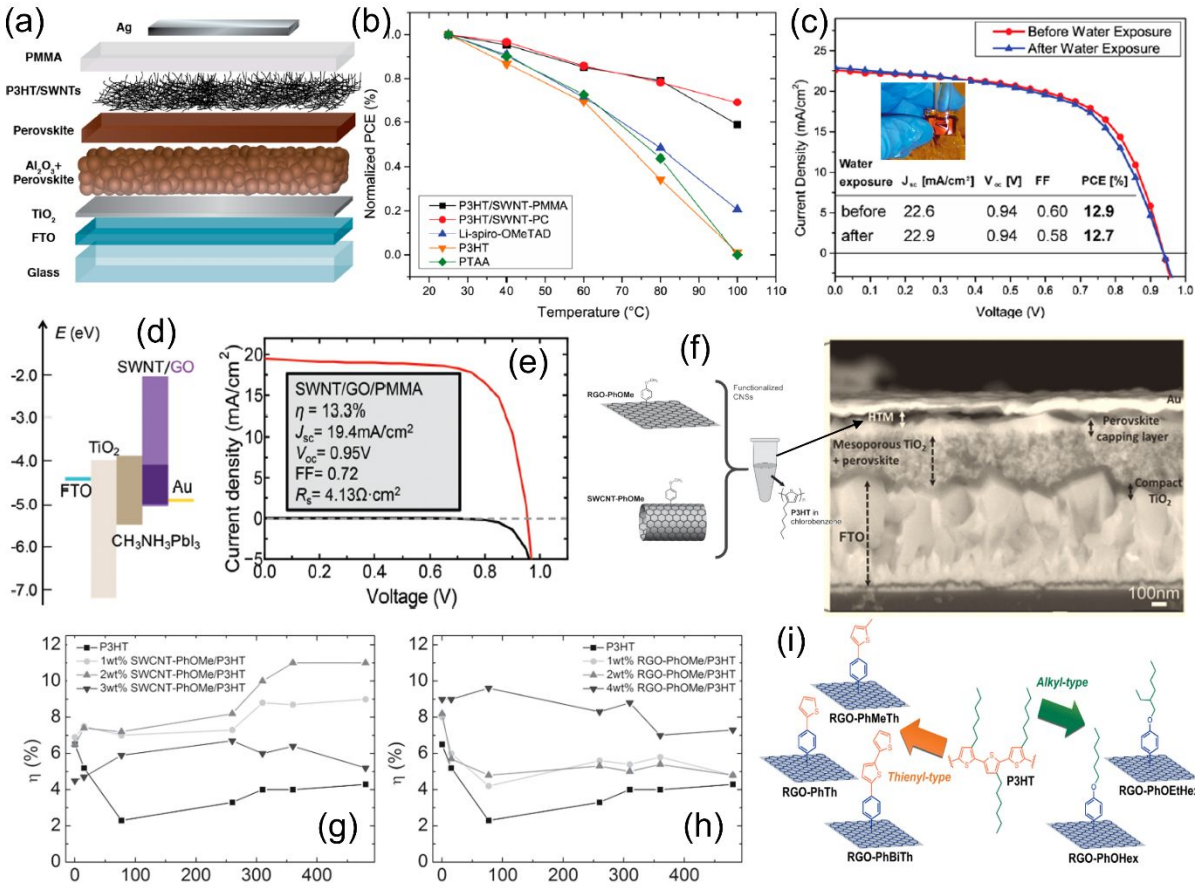

Figure 10 (a) Schematic illustration of the solar cell with a carbon nanotube-polymer composite as hole-transporting structure, (b) Power conversion efficiency for perovskite solar cells employing the range of hole-extraction layers as a function of temperature, (c) Current density−voltage plots measured under AM1.5 simulated sunlight of 100 mW cm^{-2} irradiance of the a complete perovskite solar cell employing a SWNT-P3HT-PC hole-extraction layer before and after being placed under the running water for 60 s, inset is a photograph of the same perovskite solar cell placed under a flowing tap with the active layer on top. Reproduced with permission.[17] Copyright 2014, American Chemical Society, (d) band alignment in a perovskite/SWNT/GO solar cell, (e)*J-V* curve of a perovskite solar cell using SWNT-GO-PMMA as HTL under light (red solid line) and in the dark (black solid line). Reproduced with permission.[99] Copyright 2016, Royal Society of Chemistry. (f) left: p-methoxyphenyl functionalized carbon nanostructure-P3HT blend, right: cross-sectional SEM images of a perovskite solar cell with 1 wt% rGO-PhOMe-P3HT blend HTM, (g) Endurance tests for devices based on SWCNT-PhOMe-P3HT blends, (h) Endurance tests for devices based on rGO-PhOMe-P3HT blends used as HTMs. Reproduced with permission.[88] Copyright 2016, Wiley-VCH. (i) Schematic illustration of the five types of functionalized rGO species reported in ref. Reproduced with permission.[144] Copyright 2018, Wiley-VCH.

5. Conclusions and Outlook

This review systematically summarized carbon materials-polymer composites that acting as various roles in nearly every component in PSC architectures, ranging from perovskite additives, electrodes, protective encapsulation to charge-transporter. The composite structure was designed dependent on their roles in PSCs. For instance, as hole transport materials, carbon-polymer composites can modify beneath perovskite layer for higher crystallinity and less traps or defects, alleviate energy-level gradients to improve open circuit voltage and increase conductivity of interlayer to facilitate hole extraction and transport.

Carbon-polymer composites demonstrated great potential to address the efficiency and stability issues of PSCs. Until now, among the carbon-polymer composite based devices, the highest PCE of 21.21% was reported in the one using graphene-Lewis base polymer composites as additives in perovskite[123]. This device retained 90% of its initial PCE after 480 h aging at ~35% relative humidity. Regarding the future research of carbon-polymer composite in PSCs, we propose the following prospects:

i. Investigate the transport mechanism of electrons and holes in carbon-polymer composite. Numerous studies have presented explanations of better photovoltaic performance from composite incorporation in terms of enhanced hole or electron transport and extraction. However, charge transport kinetic process in composite was not investigated. Computational simulation can be conducted to analysis the carriers migration.

ii. Characterize the interface between carbon materials and polymers. Polymers were mixed with, coated on, infiltrated in or wrapped on carbon materials to form composites. The synergic effect of carbon and polymer has been confirmed to considerably improve its conductivity, thermal and mechanical property. However, the interaction (i.e., bonding method) between carbon materials and polymers as well as its influence on

PSC device need to attract more attentions. Those fundamental understanding benefits the specific design of composite materials in PSCs.

iii. Perform *in-situ*/*operando* characterizations to analysis the functions of carbon-polymer composite. *In-situ* transmission electron microscopy, *in-situ* X-ray diffraction analysis and other advanced analysis techniques should be used to directly observe perovskite crystallization or charge transport in interlayer and interfaces of PSCs. Mechanism of composite modification should be explained better through such investigation.

List of abbreviations

photovoltaic (PV)
perovskite solar cells (PSCs)
power conversion efficiency (PCE)
formamidinium lead triiodide ($FAPbI_3$)
2,20,7,70-tetrakis-(*N*,*N*-di-*p*-methoxyphenylamine)9,90-spirobifluorene (Spiro-OMeTAD)
transparent conductive oxide (TCO)
indium tin oxide (ITO)
fluorine tin oxide (FTO)
Carbon nanomaterials (CNMs)
Reduced graphene oxide (rGO)
Graphene oxide (GO)
Carbon nanotubes (CNTs)
single walled nanotubes (SWNTs)
multi walled nanotubes (MWNTs)
Electron transport layer (ETL)
Hole transport later (HTL)
electron transport material (ETM)
hole transport material (HTM)
poly(3-hexylthiophene) (P3HT)
4-*tert*-butylpyridine (TBP)
[6,6]-phenyl-C61-butyric acid methyl ester (PCBM)

poly(3-thiophene ethanol) (PTEt)
poly(methyl methacrylate) (PMMA)
polyaniline (PANI)
poly(3,4- ethylenedioxythiophene) (PEDOT)
poly(styrenesulfonic acid) (PSSA)
polypropylene (PP)
polystyrene (PS)
polycarbonate (PC)
poly(ethylene-2,6-naphthalate) (PEN)
cross-stacked CNT (CSCNT)
Ag nanowire (AgNW)
graphene quantum dots (GQDs)
carbon quantum dots (CQDs)
carbon nanodots (CNDs)
grain boundaries (GBs)
poly[(5,6-difluoro-2,1,3-benzothiadiazol-4,7-diyl)-alt-(3,3‴-di(2-octyldodecyl)-2,2′;5′,2″;5″,2‴-quaterthiophen-5,5‴-diyl)] (PffBT4T-2OD)
polytetrafluoroethylene (PTFE)
poly(dimethylsiloxane) (PDMS)
poly(vinyl alcohol-co-ethylene) (EVOH)
poly(3,4-ethylenedioxythiophene):poly(styrene sulfonate) (PEDOT:PSS)
polythiophene (PTh)
poly(3-hexylthiophene) (P3HT)
poly(N-vinylpyrrolidone) (PVP)
polyethylenimine (PEI)
poly[bis(4-phenyl)(2,4,6-trimethylphenyl)amine] (PTAA)
p-methoxyphenyl (PhOMe)

Acknowledgements

The authors thank the support from the U.S. Department of Energy's Office of Energy Efficiency and Renewable Energy (EERE), Solar Energy Technologies Office (SETO), with award number DE-EE0009525.

References

1. S. J. Zinkle and G. Was, *Acta Materialia*, 2013, **61**, 735-758.
2. G. J. Herbert, S. Iniyan, E. Sreevalsan and S. Rajapandian, *Renewable and Sustainable Energy Reviews*, 2007, **11**, 1117-1145.
3. J. Zhang, J. Fan, B. Cheng, J. Yu and W. Ho, *Solar RRL*, 2020, **4**, 2000502.
4. P. K. Nayak, S. Mahesh, H. J. Snaith and D. Cahen, *Nature Reviews Materials*, 2019, **4**, 269-285.
5. P. You, G. Tang and F. Yan, *Materials Today Energy*, 2019, **11**, 128-158.
6. A. Kojima, K. Teshima, Y. Shirai and T. Miyasaka, *Journal of the American Chemical Society*, 2009, **131**, 6050-6051.
7. F. Bella, *Electrochimica Acta*, 2015, **175**, 151-161.
8. M. M. Lee, J. Teuscher, T. Miyasaka, T. N. Murakami and H. J. Snaith, *Science*, 2012, **338**, 643-647.
9. H.-S. Kim, C.-R. Lee, J.-H. Im, K.-B. Lee, T. Moehl, A. Marchioro, S.-J. Moon, R. Humphry-Baker, J.-H. Yum and J. E. Moser, *Scientific Reports*, 2012, **2**, 1-7.
10. N. NREL, Research-Cell Efficiencies, https://www.nrel.gov/pv/cell-efficiency.html, (accessed April, 2022).
11. M. Kim, J. Jeong, H. Lu, T. K. Lee, F. T. Eickemeyer, Y. Liu, I. W. Choi, S. J. Choi, Y. Jo and H.-B. Kim, *Science*, 2022, **375**, 302-306.
12. W. E. Sha, X. Ren, L. Chen and W. C. Choy, *Applied Physics Letters*, 2015, **106**, 221104.
13. D. Yang, R. Yang, K. Wang, C. Wu, X. Zhu, J. Feng, X. Ren, G. Fang, S. Priya and S. F. Liu, *Nature Communications*, 2018, **9**, 1-11.
14. Q. Luo, R. Wu, L. Ma, C. Wang, H. Liu, H. Lin, N. Wang, Y. Chen and Z. Guo, *Advanced Functional Materials*, 2021, **31**, 2004765.
15. J. Burschka, N. Pellet, S.-J. Moon, R. Humphry-Baker, P. Gao, M. K. Nazeeruddin and M. Grätzel, *Nature*, 2013, **499**, 316-319.
16. M. Liu, M. B. Johnston and H. J. Snaith, *Nature*, 2013, **501**, 395-398.
17. S. N. Habisreutinger, T. Leijtens, G. E. Eperon, S. D. Stranks, R. J. Nicholas and H. J. Snaith, *Nano letters*, 2014, **14**, 5561-5568.
18. V. Ferguson, S. R. P. Silva and W. Zhang, *Energy & Environmental Materials*, 2019, **2**, 107-118.
19. Y. Rong, Y. Hu, A. Mei, H. Tan, M. I. Saidaminov, S. I. Seok, M. D. McGehee, E. H. Sargent and H. Han, *Science*, 2018, **361**.

20. K. Domanski, J.-P. Correa-Baena, N. Mine, M. K. Nazeeruddin, A. Abate, M. Saliba, W. Tress, A. Hagfeldt and M. Grätzel, *ACS Nano*, 2016, **10**, 6306-6314.
21. H. Su, T. Wu, D. Cui, X. Lin, X. Luo, Y. Wang and L. Han, *Small Methods*, 2020, **4**, 2000507.
22. L. Wang, H. Zhou, J. Hu, B. Huang, M. Sun, B. Dong, G. Zheng, Y. Huang, Y. Chen and L. Li, *Science*, 2019, **363**, 265-270.
23. J.-P. Correa-Baena, M. Saliba, T. Buonassisi, M. Grätzel, A. Abate, W. Tress and A. Hagfeldt, *Science*, 2017, **358**, 739-744.
24. Z. Ku, Y. Rong, M. Xu, T. Liu and H. Han, *Scientific Reports*, 2013, **3**, 1-5.
25. N. Arora, M. I. Dar, A. Hinderhofer, N. Pellet, F. Schreiber, S. M. Zakeeruddin and M. Grätzel, *Science*, 2017, **358**, 768-771.
26. M. Li, W. W. Zuo, Q. Wang, K. L. Wang, M. P. Zhuo, H. Köbler, C. E. Halbig, S. Eigler, Y. G. Yang and X. Y. Gao, *Advanced Energy Materials*, 2020, **10**, 1902653.
27. X. Li, T. Tong, Q. Wu, S. Guo, Q. Song, J. Han and Z. Huang, *Advanced Functional Materials*, 2018, **28**, 1800475.
28. A. P. Litvin, X. Zhang, K. Berwick, A. V. Fedorov, W. Zheng and A. V. Baranov, *Renewable and Sustainable Energy Reviews*, 2020, **124**, 109774.
29. N. E. Safie, M. A. Azam, M. F. Aziz and M. Ismail, *International Journal of Energy Research*, 2021, **45**, 1347-1374.
30. M. Hadadian, J.-H. Smått and J.-P. Correa-Baena, *Energy & Environmental Science*, 2020, **13**, 1377-1407.
31. K. Moore and W. Wei, *Nano Materials Science*, 2021, **3**, 276-290.
32. F. Bonaccorso, A. Bartolotta, J. N. Coleman and C. Backes, *Advanced Materials*, 2016, **28**, 6136-6166.
33. F. Meng, A. Liu, L. Gao, J. Cao, Y. Yan, N. Wang, M. Fan, G. Wei and T. Ma, *Journal of Materials Chemistry A*, 2019, **7**, 8690-8699.
34. Y. Gao, *Nanoscale research letters*, 2017, **12**, 1-17.
35. M. Batmunkh, C. J. Shearer, M. J. Biggs and J. G. Shapter, *Journal of Materials Chemistry A*, 2015, **3**, 9020-9031.
36. Y. Bai, X. Meng and S. Yang, *Advanced Energy Materials*, 2018, **8**, 1701883.
37. F. Wang, Y. Cao, C. Chen, Q. Chen, X. Wu, X. Li, T. Qin and W. Huang, *Advanced Functional Materials*, 2018, **28**, 1803753.

38. V. D'innocenzo, G. Grancini, M. J. Alcocer, A. R. S. Kandada, S. D. Stranks, M. M. Lee, G. Lanzani, H. J. Snaith and A. Petrozza, *Nature Communications*, 2014, **5**, 1-6.
39. S. Kim, H. S. Lee, J. M. Kim, S. W. Seo, J. H. Kim, C. W. Jang and S.-H. Choi, *Journal of Alloys and Compounds*, 2018, **744**, 404-411.
40. K. Petridis, G. Kakavelakis, M. M. Stylianakis and E. Kymakis, *Chemistry–An Asian Journal*, 2018, **13**, 240-249.
41. P.-C. Hsu, D. Kong, S. Wang, H. Wang, A. J. Welch, H. Wu and Y. Cui, *Journal of the American Chemical Society*, 2014, **136**, 10593-10596.
42. S. De, P. E. Lyons, S. Sorel, E. M. Doherty, P. J. King, W. J. Blau, P. N. Nirmalraj, J. J. Boland, V. Scardaci and J. Joimel, *ACS Nano*, 2009, **3**, 714-720.
43. H.-Z. Geng, K. K. Kim, K. P. So, Y. S. Lee, Y. Chang and Y. H. Lee, *Journal of the American Chemical Society*, 2007, **129**, 7758-7759.
44. T. Minami, *Thin Solid Films*, 2008, **516**, 5822-5828.
45. S. He, L. Qiu, D.-Y. Son, Z. Liu, E. J. Juarez-Perez, L. K. Ono, C. Stecker and Y. Qi, *ACS Energy Letters*, 2019, **4**, 2032-2039.
46. W.-J. Yin, T. Shi and Y. Yan, *Applied Physics Letters*, 2014, **104**, 063903.
47. N. Aristidou, I. Sanchez-Molina, T. Chotchuangchutchaval, M. Brown, L. Martinez, T. Rath and S. A. Haque, *Angewandte Chemie*, 2015, **127**, 8326-8330.
48. M. Grätzel, *Nature Materials*, 2014, **13**, 838-842.
49. M. A. Green, A. Ho-Baillie and H. J. Snaith, *Nature Photonics*, 2014, **8**, 506-514.
50. R. Wang, M. Mujahid, Y. Duan, Z. K. Wang, J. Xue and Y. Yang, *Advanced Functional Materials*, 2019, **29**, 1808843.
51. J. Niu, D. Yang, X. Ren, Z. Yang, Y. Liu, X. Zhu, W. Zhao and S. F. Liu, *Organic Electronics*, 2017, **48**, 165-171.
52. M. Jørgensen, K. Norrman and F. C. Krebs, *Solar Energy Materials and Solar Cells*, 2008, **92**, 686-714.
53. D. B. Kim, J. C. Yu, Y. S. Nam, D. W. Kim, E. D. Jung, S. Y. Lee, S. Lee, J. H. Park, A.-Y. Lee and B. R. Lee, *Journal of Materials Chemistry C*, 2016, **4**, 8161-8165.
54. Z. Wu, S. Bai, J. Xiang, Z. Yuan, Y. Yang, W. Cui, X. Gao, Z. Liu, Y. Jin and B. Sun, *Nanoscale*, 2014, **6**, 10505-10510.
55. E. Jokar, Z. Y. Huang, S. Narra, C. Y. Wang, V. Kattoor, C. C. Chung and E. W. G. Diau, *Advanced Energy Materials*, 2018, **8**, 1701640.

56. M. Z. Iqbal, J. U. Nabi, S. Siddique, H. T. A. Awan, S. S. Haider and M. Sulman, *International Journal of Energy Research*, 2020, **44**, 1464-1487.
57. J.-S. Yeo, R. Kang, S. Lee, Y.-J. Jeon, N. Myoung, C.-L. Lee, D.-Y. Kim, J.-M. Yun, Y.-H. Seo and S.-S. Kim, *Nano Energy*, 2015, **12**, 96-104.
58. P. You, Z. Liu, Q. Tai, S. Liu and F. Yan, *Advanced Materials*, 2015, **27**, 3632-3638.
59. Z. Zhu, J. Ma, Z. Wang, C. Mu, Z. Fan, L. Du, Y. Bai, L. Fan, H. Yan and D. L. Phillips, *Journal of the American Chemical Society*, 2014, **136**, 3760-3763.
60. Q. Luo, H. Ma, Q. Hou, Y. Li, J. Ren, X. Dai, Z. Yao, Y. Zhou, L. Xiang and H. Du, *Advanced Functional Materials*, 2018, **28**, 1706777.
61. D. Bogachuk, S. Zouhair, K. Wojciechowski, B. Yang, V. Babu, L. Wagner, B. Xu, J. Lim, S. Mastroianni and H. Pettersson, *Energy & Environmental Science*, 2020, **13**, 3880-3916.
62. S. Wang, Z. Zhang, Z. Tang, C. Su, W. Huang, Y. Li and G. Xing, *Nano Energy*, 2021, **82**, 105712.
63. D. M. Jones, J. Hidalgo, Y. An, C. Evans, J. Vagott and J.-P. Correa-Baena, *Journal of Materials Chemistry C*, 2021.
64. W. Hou, Y. Xiao, G. Han and J.-Y. Lin, *Polymers*, 2019, **11**, 143.
65. W. Chee, H. Lim, N. Huang and I. Harrison, *RSC Advances*, 2015, **5**, 68014-68051.
66. K. S. Novoselov, A. K. Geim, S. V. Morozov, D.-e. Jiang, Y. Zhang, S. V. Dubonos, I. V. Grigorieva and A. A. Firsov, *Science*, 2004, **306**, 666-669.
67. Z. Chen, Y. Qi, X. Chen, Y. Zhang and Z. Liu, *Advanced Materials*, 2019, **31**, 1803639.
68. C. Lee, X. Wei, J. W. Kysar and J. Hone, *Science*, 2008, **321**, 385-388.
69. K. I. Bolotin, K. J. Sikes, Z. Jiang, M. Klima, G. Fudenberg, J. Hone, P. Kim and H. Stormer, *Solid State Communications*, 2008, **146**, 351-355.
70. A. A. Balandin, S. Ghosh, W. Bao, I. Calizo, D. Teweldebrhan, F. Miao and C. N. Lau, *Nano Letters*, 2008, **8**, 902-907.
71. F. Bonaccorso, Z. Sun, T. Hasan and A. Ferrari, *Nature Photonics*, 2010, **4**, 611-622.
72. S. Javaid, C. W. Myung, S. Pourasad, B. Rakshit, K. S. Kim and G. Lee, *Journal of Materials Chemistry A*, 2018, **6**, 18635-18640.
73. Y. Zhu, S. Murali, W. Cai, X. Li, J. W. Suk, J. R. Potts and R. S. Ruoff, *Advanced Materials*, 2010, **22**, 3906-3924.
74. O. C. Compton and S. T. Nguyen, S*mall*, 2010, **6**, 711-723.

75. R. Tarcan, O. Todor-Boer, I. Petrovai, C. Leordean, S. Astilean and I. Botiz, *Journal of Materials Chemistry C*, 2020, **8**, 1198-1224.
76. S. Iijima, *Nature*, 1991, **354**, 56-58.
77. G. Mittal, V. Dhand, K. Y. Rhee, S.-J. Park and W. R. Lee, *Journal of Industrial and Engineering Chemistry*, 2015, **21**, 11-25.
78. C. Xia, S. Zhu, T. Feng, M. Yang and B. Yang, *Advanced Science*, 2019, **6**, 1901316.
79. Z. Kang and S.-T. Lee, *Nanoscale*, 2019, **11**, 19214-19224.
80. Q. Guo, F. Yuan, B. Zhang, S. Zhou, J. Zhang, Y. Bai, L. Fan, T. Hayat, A. Alsaedi and Z. a. Tan, *Nanoscale*, 2019, **11**, 115-124.
81. Z. Wang, F. Yuan, W. Sun, H. Shi, T. Hayat, A. Alsaedi, L. Fan and Z. a. Tan, *Advanced Optical Materials*, 2019, **7**, 1901299.
82. X. Guo, B. Zhao, K. Xu, S. Yang, Z. Liu, Y. Han, J. Xu, D. Xu, Z. Tan and S. Liu, *Small*, 2021, **17**, 2102272.
83. A. Cayuela, M. Soriano, C. Carrillo-Carrión and M. Valcárcel, *Chemical Communications*, 2016, **52**, 1311-1326.
84. G. S. Han, J. S. Yoo, F. Yu, M. L. Duff, B. K. Kang and J.-K. Lee, *Journal of Materials Chemistry A*, 2017, **5**, 14733-14740.
85. X. Zheng, H. Chen, Z. Wei, Y. Yang, H. Lin and S. Yang, *Frontiers of Optoelectronics*, 2016, **9**, 71-80.
86. A. Giuri, S. Masi, S. Colella, A. Listorti, A. Rizzo, A. Kovtun, S. Dell'Elce, A. Liscio and C. Esposito Corcione, *Polymer Engineering & Science*, 2017, **57**, 546-552.
87. A. Kumar, K. Sharma and A. R. Dixit, *Carbon Letters*, 2021, **31**, 149-165.
88. T. Gatti, S. Casaluci, M. Prato, M. Salerno, F. Di Stasio, A. Ansaldo, E. Menna, A. Di Carlo and F. Bonaccorso, *Advanced Functional Materials*, 2016, **26**, 7443-7453.
89. J. W. Jung, S. H. Son and J. Choi, *Polymers*, 2021, **13**, 1281.
90. F. Barroso-Bujans, S. Cerveny, R. Verdejo, J. d. del Val, J. M. Alberdi, A. Alegría and J. Colmenero, *Carbon*, 2010, **48**, 1079-1087.
91. H. Mohseni, M. Dehghanipour, N. Dehghan, F. Tamaddon, M. Ahmadi, M. Sabet and A. Behjat, *Solar Energy*, 2021, **213**, 59-66.
92. S. W. Tong, J. Balapanuru, D. Fu and K. P. Loh, *ACS Applied Materials & Interfaces*, 2016, **8**, 29496-29503.
93. S. Cogal, L. Calio, G. C. Cogal, M. Salado, S. Kazim, L. Oksuz, S. Ahmad and A. U. Oksuz, *Polymer Bulletin*, 2018, **75**, 4531-4545.

94. P. Pötschke, A. R. Bhattacharyya and A. Janke, *European PolymerJjournal*, 2004, **40**, 137-148.
95. J. Y. Kim and S. H. Kim, *Journal of Polymer Science Part B: Polymer Physics*, 2006, **44**, 1062-1071.
96. B. Shen, W. Zhai, M. Tao, D. Lu and W. Zheng, *Composites Science and Technology*, 2013, **86**, 109-116.
97. E. Nilsson, H. Oxfall, W. Wandelt, R. Rychwalski and B. Hagström, *Journal of Applied Polymer Science*, 2013, **130**, 2579-2587.
98. Y. Zhou, X. Yin, Q. Luo, X. Zhao, D. Zhou, J. Han, F. Hao, M. Tai, J. Li and P. Liu, *ACS Applied Materials & Interfaces*, 2018, **10**, 31384-31393.
99. F. Wang, M. Endo, S. Mouri, Y. Miyauchi, Y. Ohno, A. Wakamiya, Y. Murata and K. Matsuda, *Nanoscale*, 2016, **8**, 11882-11888.
100. H. Dong, Z. Wu, Y. Jiang, W. Liu, X. Li, B. Jiao, W. Abbas and X. Hou, *ACS Applied Materials & Interfaces*, 2016, **8**, 31212-31221.
101. S. Qin, C. Chen, M. Cui, A. Zhang, H. Zhao and L. Wang, *RSC Advances*, 2017, **7**, 3003-3011.
102. J. Wang, F. Song, Y. Ding and M. Shao, *Materials & Design*, 2020, **195**, 109073.
103. P. Govindaraj, B. Fox, P. Aitchison and N. Hameed, *Industrial & Engineering Chemistry Research*, 2019, **58**, 17106-17129.
104. R. Bauld, D.-Y. W. Choi, P. Bazylewski, R. Divigalpitiya and G. Fanchini, *Journal of Materials Chemistry C*, 2018, **6**, 2901-2914.
105. W. Park, J. Hu, L. A. Jauregui, X. Ruan and Y. P. Chen, *Applied Physics Letters*, 2014, **104**, 113101.
106. H. Wang, Q. Hao, X. Yang, L. Lu and X. Wang, *Electrochemistry Communications*, 2009, **11**, 1158-1161.
107. S. Mabrouk, B. Bahrami, H. Elbohy, K. M. Reza, A. Gurung, M. Liang, F. Wu, M. Wang, S. Yang and Q. Qiao, *InfoMat*, 2020, **2**, 928-941.
108. Q. Li, Y. Guo, W. Li, S. Qiu, C. Zhu, X. Wei, M. Chen, C. Liu, S. Liao and Y. Gong, *Chemistry of Materials*, 2014, **26**, 4459-4465.
109. Y.-F. Zhang, Y.-J. Ren and S.-L. Bai, *International Journal of Heat and Mass Transfer*, 2018, **118**, 510-517.
110. A. Yu, P. Ramesh, M. E. Itkis, E. Bekyarova and R. C. Haddon, *The Journal of Physical Chemistry C*, 2007, **111**, 7565-7569.

111. W. Guo and G. Chen, *Journal of Applied Polymer Science*, 2014, **131**.
112. K. M. Shahil and A. A. Balandin, *Nano Letters*, 2012, **12**, 861-867.
113. M. A. García and J. Balenzategui, *Renewable Energy*, 2004, **29**, 1997-2010.
114. X. Ji, Y. Xu, W. Zhang, L. Cui and J. Liu, *Composites Part A: Applied Science and Manufacturing*, 2016, **87**, 29-45.
115. D. Qian, E. C. Dickey, R. Andrews and T. Rantell, *Applied Physics Letters*, 2000, **76**, 2868-2870.
116. Q. Zhao, Y. Shen, M. Ji, L. Zhang, T. Jiang and C. Li, *Journal of Industrial and Engineering Chemistry*, 2014, **20**, 544-548.
117. N. Rajamanickam, S. Kumari, V. K. Vendra, B. W. Lavery, J. Spurgeon, T. Druffel and M. K. Sunkara, *Nanotechnology*, 2016, **27**, 235404.
118. N. Ahn, I. Jeon, J. Yoon, E. I. Kauppinen, Y. Matsuo, S. Maruyama and M. Choi, *Journal of Materials Chemistry A*, 2018, **6**, 1382-1389.
119. H. W. Lee, Y. Yoon, S. Park, J. H. Oh, S. Hong, L. S. Liyanage, H. Wang, S. Morishita, N. Patil and Y. J. Park, *Nature Communications*, 2011, **2**, 1-8.
120. R. Sarvari, S. Agbolaghi and B. Massoumi, *Optical Materials*, 2019, **92**, 81-86.
121. C. Eames, J. M. Frost, P. R. Barnes, B. C. O'regan, A. Walsh and M. S. Islam, *Nature Communications*, 2015, **6**, 1-8.
122. Y. Shao, Y. Fang, T. Li, Q. Wang, Q. Dong, Y. Deng, Y. Yuan, H. Wei, M. Wang and A. Gruverman, *Energy & Environmental Science*, 2016, **9**, 1752-1759.
123. Q. Lou, G. Lou, R. Peng, Z. Liu, W. Wang, M. Ji, C. Chen, X. Zhang, C. Liu and Z. Ge, *ACS Applied Energy Materials*, 2021, **4**, 3928-3936.
124. X. Xu, Q. Chen, Z. Hong, H. Zhou, Z. Liu, W.-H. Chang, P. Sun, H. Chen, N. D. Marco and M. Wang, *Nano Letters*, 2015, **15**, 6514-6520.
125. Y. Rong, Y. Hu, A. Mei, H. Tan, M. I. Saidaminov, S. I. Seok, M. D. McGehee, E. H. Sargent and H. Han, *Science*, 2018, **361**, eaat8235.
126. A. Guerrero, J. You, C. Aranda, Y. S. Kang, G. Garcia-Belmonte, H. Zhou, J. Bisquert and Y. Yang, *ACS Nano*, 2016, **10**, 218-224.
127. J. H. Jang, B.-J. Kim, J.-h. Kim, E. Han, E. Y. Choi, C. H. Ji, K.-T. Kim, J. Kim and N. Park, *ACS Omega*, 2019, **4**, 9211-9218.
128. J. Xu, K. Wang, S.-Z. Zu, B.-H. Han and Z. Wei, *ACS Nano*, 2010, **4**, 5019-5026.
129. Y.-C. Yong, X.-C. Dong, M. B. Chan-Park, H. Song and P. Chen, *ACS Nano*, 2012, **6**, 2394-2400.

130. J. Yang, B. D. Siempelkamp, E. Mosconi, F. De Angelis and T. L. Kelly, *Chemistry of Materials*, 2015, **27**, 4229-4236.
131. D.-Y. Lee, S.-I. Na and S.-S. Kim, *Nanoscale*, 2016, **8**, 1513-1522.
132. C. Redondo-Obispo, T. S. Ripolles, S. Cortijo-Campos, A. L. Alvarez, E. Climent-Pascual, A. de Andrés and C. Coya, *Materials & Design*, 2020, **191**, 108587.
133. Q.-Q. Chu, B. Ding, J. Peng, H. Shen, X. Li, Y. Liu, C.-X. Li, C.-J. Li, G.-J. Yang and T. P. White, *Journal of Materials Science & Technology*, 2019, **35**, 987-993.
134. J. Ye, X. Li, J. Zhao, X. Mei and Q. Li, *RSC Advances*, 2016, **6**, 36356-36361.
135. J. C. Yu, J. A. Hong, E. D. Jung, D. B. Kim, S.-M. Baek, S. Lee, S. Cho, S. S. Park, K. J. Choi and M. H. Song, *Scientific Reports*, 2018, **8**, 1-9.
136. H. Guo, X. Huang, B. Pu, J. Yang, H. Chen, Y. Zhou, J. Yang, Y. Li, Z. Wang and X. Niu, *RSC Advances*, 2017, **7**, 50410-50419.
137. S.-P. Cho, G. Han, Y.-H. Seo, Y.-J. Noh, J.-Y. Sohn, I.-T. Hwang, J. Shin, C.-H. Jung and S.-I. Na, *Composites Science and Technology*, 2021, **201**, 108548.
138. J. S. Cho, W. Jang, S. C. Mun, M. Yi, J. H. Park and D. H. Wang, *Carbon*, 2018, **139**, 564-571.
139. W. Li, N. Cheng, Y. Cao, Z. Zhao, Z. Xiao, W. Zi and Z. Sun, *Organic Electronics*, 2020, **78**, 105575.
140. Z. Li, C. Liu, X. Zhang, J. Guo, H. Cui, L. Shen, Y. Bi and W. Guo, *Materials Today Energy*, 2019, **12**, 161-167.
141. S. N. Habisreutinger, T. Leijtens, G. E. Eperon, S. D. Stranks, R. J. Nicholas and H. J. Snaith, *The Journal of Physical Chemistry Letters*, 2014, **5**, 4207-4212.
142. S. N. Habisreutinger, B. Wenger, H. J. Snaith and R. J. Nicholas, *ACS Energy Letters*, 2017, **2**, 622-628.
143. G. Wang, J. Liu, K. Chen, R. Pathak, A. Gurung and Q. Qiao, *Journal of Colloid and Interface Science*, 2019, **555**, 180-186.
144. T. Gatti, F. Lamberti, P. Topolovsek, M. Abdu-Aguye, R. Sorrentino, L. Perino, M. Salerno, L. Girardi, C. Marega and G. A. Rizzi, *Solar RRL*, 2018, **2**, 1800013.

Table 1. Summary and comparation of preparation methods for carbon-polymer composites.

Methods	Advantages	Challenges
Solution blending	• Simple and commonly used • Feasible for large scale production	▪ Requires large volume of organic solvents and may cause high cost ▪ Residual solvents may influence properties of composite
In-situ polarization	• Deal with insoluble and unstable polymers • Strong interaction between carbon materials and polymer	▪ Difficult to control the level of polymerization
Melt processing	• Environmentally friendly • Thermoplastic polymers	▪ Hard to form uniform dispersion ▪ Polymer degradation due to high temperature
Coating	• Simple and practical • Various choices for coating techniques	▪ Layer-by-layer may not homogeneous

Table 2 Summary of device configurations and PV performances for PSCs using carbon-polymer composite as additives, electrode and encapsulation layer.

Role	Composite materials	Perovskite	Electrode/ETL	HTL/electrode	PCE (%)	J_{sc} (mA)	V_{oc} (V)	FF (%)	Stability	Ref.
Additive in perovskite layer	*graphene-PANI*	$CH_3NH_3PbI_3$	FTO /TiO_2	CuI/Au	/	/	/	/	<10% decrease, 96 h, 99%RH	[117]
	rGO-P3HT	$CH_3NH_3PbI_3$	FTO/b-TiO_2/mp-TiO_2	spiro-OMeTAD/MoO_3/Ag	15.1	22	0.95	72	N/A	[120]
	Graphene-PM7	$Cs0._{05}FA_{0.79}MA_{0.16}PbI_{2.49}Br_{0.5}$	ITO/SnO_2	spiro-OMeTAD/Ag	21.2	24	1.16	76	10% decrease 480 h, 35%RH	[123]
	CNT-PTAA	$CH_3NH_3PbI_3$	ITO/C_{60}	CNT-PTAA	15.3	23	0.98	67	N/A	[118]
Electrode	*Graphene-PEDOT:PSS*	$CH_3NH_3PbI_{3x}Cl_x$	FTO / TiO_2	spiro-OMeTAD/PEDOT:PSS-Graphene	12.3	19	0.96	67	N/A	[58]
	MG-A-P	$CH_3NH_3PbI_3$	Ag/BCP/ PCBM	MoO_3/ MG-A-P	10.4	/	/	/	N/A	[100]
	CSCNT-PEI	$MAPbI_3$	CSCNT-PEI/PCBM	NiO_x/FTO	10.8	18	0.95	61	94% remain 500h	[98]
	CNT-P3HT	$CH_3NH_3PbI_3$	FTO/c-TiO_2/m-TiO_2	CNT-P3HT	13.4	22	0.91	65	97% remain 40day	[85]
Encapsulation Layer	*rGO-PMMA*	$CH_3NH_3PbI_3$	FTO/mp-TiO_2	spiro-OMeTAD/Au	15.7	22	1.01	0.68	100% remain 1000h, air	[84]
	EVOH-GO-SiO_2	$CH_3NH_3PbI_3$	FTO/TiO_2/	spiro-OMeTAD/Au	17.3	23	1.1	67	86% remain 5 h touch water	[127]

Table 3 Summary of device configurations and PV performances for PSCs using carbon-polymer composite as charge transport layer.

Role	Composite materials	Perovskite	Electrode /ETL	HTL/electrode	PCE (%)	J_{sc} (mA)	V_{oc} (V)	FF (%)	Stability	Ref
HTL	*graphene doped PEDOT:PSS*	$MAPbI_3$	ITO/ PCBM	graphene doped PEDOT:PSS /Al	/	/	/	/	N/A	[132]
	Graphene-P3HT	$FA_{0.3}MA_{0.7}PbI_3$	FTO/SnO_2@TiO_2	Graphene-P3HT/Carbon	18.1	22	1.09	74	97% remain 600h	[133]
	F-graphene doped P3HT	$CH_3NH_3PbI_3$	FTO/TiO_2	F-graphene-P3HT/Ag	13.8	19	0.99	71	70% remain 8 weeks	[134]
	GO-PEDOT:PSS	$CH_3NH_3PbI_3$	Ag/PCBM	GO-PEDOT:PSS/ITO	9.74	15	0.84	73	Stable up 48 h	[131]
	GO doped PEDOT:PSS	$CH_3NH_3PbI_3$	Ag/PCBM	GO-PEDOT:PSS/ITO	14.2	20	0.9	79	N/A	[51]
	sGO-PEDOT:PSS	$CH_3NH_3PbI_3$	Ag/PCBM	sGO-PEDOT:PSS/ITO	13.9	19	1.0	67	N/A	[136]
	GO-PEDOT:PSS	$CH_3NH_3PbI_3$	Ag/ PCBM	GO-PEDOT:PSS/ITO	18.1	21	1.02	82	80% remain 25 days	[135]
	γ-ray-GO-PEDOT:PSS	$CH_3NH_3PbI_3$	Al/PCBM	γ-ray-GO-PEDOT:PSS/ITO	12.7	18	1.0	74	N/A	[138]
	GO-PEDOT:PSS-PANI	$CH_3NH_3PbI_3$	Ag/PCBM	GO-PEDOT:PSS-PANI/ITO	18.1	23	1.05	75	25% remain 80 days	[107]
	SWCNT-PhOMe-P3HT	$CH_3NH_3PbI_3$	FTO/TiO_2	SWCNT-PhOMe-P3HT /Au	11.6	22	0.62	85	8.7% 3240h endurance test	[88]
	rGO-PhOMe-P3HT	$CH_3NH_3PbI_3$	FTO/TiO_2	rGO-PhOMe/P3HT /Au	10	19	0.62	86	4.7% 3240h endurance test	[88]
	Functionalized rGO-P3HT	$Cs_{0.15}FA_{0.8}5PbI_3$	FTO/C_{60}	Functionalized rGO-P3HT/Au	9.8	/	/	/	N/A	[144]

	I_2 doped PEDOT-Graphene	$FAPbI_3)_{0.85}(MAPbBr_3)_{0.15}$	FTO/TiO_2	I_2 doped PEDOT-Graphene /Au	8.79	21	0.79	52	72% remain 180 days	93
	rGO-PVP	$CH_3NH_3PbI_3$	Au/PCBM	rGO-PVP/ITO	11.36	15	0.97	80	50% remain 1000 h	137
	rGO-PANI	$CH_3NH_3PbI_3$	Ag/BCP/PCBM	rGO-PANI/ ITO	16.6	22	1.0	74	87% remain 500h	89
	GQDs-PEDOT:PSS	$CH_3NH_3PbI_3$	Ag/PCBM	GQDs-PEDOT:PSS /FTO	15.24	21	0.995	71	77% remain 9 days	139
	CNDs-PEDOT:PSS	$CH_3NH_3PbI_3$	Ag/PCBM+BCP	CNDs-PEDOT:PSS/ITO	18.03	22.6	1.01	79	70% remain 60 days	140
	SWNT-GO-PMMA	$CH_3NH_3PbI_3$	FTO/c-TiO_2/m-TiO_2	SWNT-GO-PMMA/Au	13.3	19	0.95	72	98% reman 10 days, 70-80% RH	99
	SWNT-P3HT-PMMA	$CH_3NH_3PbI_3$	FTO/TiO_2 /Al_2O_3	SWNT-P3HT-PMMA/Ag	15.3	23	1.02	66	~10% drop 80^0C, 96h	17
	SWNT-P3HT	$CH_3NH_3PbI_3$	FTO/TiO_2	SWNT-P3HT/spiro-OMeTAD /Ag	15.4	21	1.02	71	N/A	141
	SWNT-P3HT	$FA_{0.83}MA_{0.17}Pb(I_{0.87}Br_{0.17})_3$	FTO/SnO_2	SWNT-P3HT/ spiro-OMeTAD/Ag	18.8	22	1.14	75	N/A	142
	MWCNT-P3HT	$CsPbI_2Br$	FTO/TiO_2 /	MWCNT-P3HT/Carbon	10.0	13	1.21	62	85% remain 250h	143
ETL	*rGO-PANI*	$CsMAFAPbI_3$	FTO /mp-TiO_2+ rGO-PANI	spiro-OMeTAD/Au	16.5	26	0.96	63	82% remain 1870h	91
	mp-GP	$CH_3NH_3PbI_3$	ITO/mp-GP/ Cs_2CO_3	PffBT4T-2OD/Ag	13.8	/	/	/	88% remain 200h	92